Planar laser imaging of differential molecular diffusion in gas-phase turbulent jets

C. J. Brownell and L. K. Su[a)]
Applied Fluid Imaging Laboratory, Department of Mechanical Engineering, Johns Hopkins University, Baltimore, Maryland 21218, USA

(Received 31 August 2007; accepted 27 January 2008; published online 18 March 2008)

Planar laser Rayleigh scattering yields quantitative, two-dimensional measurements of differential diffusion in a turbulent propane-helium jet issuing into air. The jet exit Reynolds number ranges from 1000 to 3000, corresponding to estimated outer-scale Reynolds numbers from 4300 to 13 000. Using a technique originally proposed by Bilger and Dibble [Combust. Sci. Technol. **28**, 161 (1982)], the imaging measurements allow direct determination of a normalized scalar difference quantity ξ. For the lower Re, significant differential diffusion develops in the pretransitional portion of the flow. Downstream of the turbulent transition, radial profiles of mean ξ take on a characteristic form, with an excess of the less-diffusive propane on the jet boundary. This characteristic form is independent of Reynolds number, and is thus apparently independent of the degree of differential diffusion in the pretransition range. Evolution of the ξ fields in the turbulent part of the flow is surprisingly consistent with the mixing of conventional scalar quantities. Fluctuation profiles of ξ have a self-similar, bimodal shape for each Re, and power spectra of ξ are monotonically decreasing, with a distinct $k^{-5/3}$ inertial range. This spectral form is at odds with prior analytical and computational results in isotropic turbulence, which predicted that the spectrum would show a peak intermediate between the diffusive cutoffs of the individual scalars. The discrepancy appears to be due to the forcing applied in the simulations; the differential diffusion in the experiments preferentially develops in the jet near field, so the resulting evolution is more akin to a decay process. This is further emphasized by the observation that the thickness of ξ structures in the jet decreases with downstream distance. The present results indicate that consideration of differential diffusion must account for the details of the flow configuration, particularly the uniformity of turbulence levels. This has important implications for reacting flows, where local laminarization by heat release can be significant. © *2008 American Institute of Physics*. [DOI: 10.1063/1.2884465]

I. INTRODUCTION

Simulations of turbulent nonpremixed flames are complicated by the presence of many distinct chemical species, each with unique physical properties and, in particular, highly disparate values of molecular diffusivity. To make these flames computationally tractable, a common simplification is to represent the fuel/oxidizer mixing using the mixture fraction, which is a single conserved scalar from which the entire thermochemical state of a system can be determined. This approach assumes that, in turbulence, inertial effects dominate diffusive effects, thus rendering the differences in diffusivity values irrelevant. However, this assumption is of questionable validity, owing to the nature of the mixing in turbulent combustion. The molecular mixing that is the necessary precursor to chemical reactions takes place at the smallest flow scales, which is precisely where diffusive effects remain important even when flow Reynolds numbers are high. The impact of variations in diffusivity on a reacting flow were observed experimentally by Drake *et al.*,[1] and formulated theoretically by Bilger.[2] There have since been numerous studies of the impact of differential diffusion on turbulent nonpremixed flames, which have investigated such aspects of the flames as elemental mixture fractions[3] and observed flame temperatures.[4]

In order to study differential diffusion without the complications of heat release and chemical reaction, Bilger and Dibble[5] proposed an experiment employing a Rayleigh scattering diagnostic method in a nonreacting hydrogen-propane jet flowing into air. In that experiment, the Rayleigh scattering cross section of the jet mixture is matched to the surrounding air, so any differential diffusion of the hydrogen and propane as the flow evolves is measured directly in terms of variations in the local scattering cross section of the fluid. Several applications of this basic experimental arrangement have been documented in the literature. Kerstein *et al.*[6] presented one-dimensional measurements of differential diffusion in a hydrogen-freon jet. That work demonstrated the validity of using the Rayleigh scattering method to study differential diffusion, and provided quantitative measurements of differential diffusion in nonreacting jets at Re=20 000. Dibble and Long[7] recently documented two-dimensional imaging measurements of the same hydrogen-freon flow. That paper notably describes the sensitive nature of the experiment, particularly in controlling the flow rates of the jet gases, and discusses methods for reducing experimental uncertainties.

[a)]Author to whom correspondence should be addressed. Electronic mail: lsu@jhu.edu. Telephone: 410–516–8637. Fax: 410–516–7254.

Other experimental and numerical studies have focused on quantifying differential diffusion in nonreacting flows. Long *et al.*[8] demonstrated an alternative experimental method to that proposed by Bilger and Dibble, instead using simultaneous planar laser-induced fluorescence and Mie scattering to capture the difference between the combined turbulent and molecular diffusion of a fluorescent, molecular tracer (biacetyl) and the turbulent diffusion of seeded particulates. From measurements in a dyed water jet, Saylor and Sreenivasan[9] showed that observations of "unmixing" from these prior gas-phase measurements were not simply due to inertial separation. Lavertu *et al.*[10] similarly considered differential diffusion in high Schmidt number jets. Several papers have studied the dependence of differential diffusion on Reynolds number,[10–13] but there exists no consensus on a specific Re dependence. Various authors have also used direct numerical simulation (DNS) methods to study differential diffusion in isotropic turbulence,[13–20] and as a result there exists a wealth of data for comparison purposes.

This paper presents results from an experiment based on the arrangement proposed by Bilger and Dibble. In an axisymmetric, turbulent co-flowing jet, we use planar laser Rayleigh scattering to obtain imaging measurements of the differential diffusion between helium and propane jet fluids as they mix with the surrounding air. The measured quantity is the differential diffusion parameter ξ, defined as the local difference between the normalized helium and propane mole fractions, namely,

$$\xi = \frac{X_{C_3H_8}}{X^0_{C_3H_8}} - \frac{X_{He}}{X^0_{He}}, \tag{1}$$

where $X^0_{C_3H_8}$ and X^0_{He} are the respective initial mole fractions of the propane and helium. This parameter ξ alone cannot be used to determine the concentrations of the three distinct species in the flow, but it is useful in examining differences in the evolution of two initially mixed species. (More general methods of quantifying differential diffusion have been proposed,[21] but are not suitable for the present experiment.)

The transport equation for the mole fraction of each species i is written

$$\frac{\partial X_i}{\partial t} + \nabla \cdot (X_i \mathbf{u}) - \nabla \cdot D_i \nabla X_i = 0, \tag{2}$$

using the customary assumption (e.g., Bilger and Dibble[5]) that the multicomponent diffusion effects are negligible; i.e., that the mass diffusivity D_i is uniform regardless of the local fluid composition. Equation (2) is valid for variable-density flows provided that density fluctuations are small; namely, $|\nabla \rho / \rho| \ll 1$. The transport equation for ξ is, then,

$$\frac{\partial \xi}{\partial t} + \nabla \cdot (\xi \mathbf{u}) - \nabla \cdot D_{C_3H_8} \nabla \xi = -\nabla \cdot [(D_{He} - D_{C_3H_8}) \frac{\nabla X_{He}}{X^0_{He}}, \tag{3}$$

where, as with Eq. (2), the left side of the equation includes the advective and diffusive terms, but the right side now has a source term that relates to the difference in the diffusivities D_i. This source term means that the properties of the parameter ξ may differ in notable ways from those of conventional conserved scalars such as the mole fractions X_i.

Through quantitative analysis of the resulting two-dimensional data, we are able to study structural characteristics of differential diffusion that have previously been accessible only to computations. Because the sizes of scalar mixing structures are determined from a balance between local strain and diffusion, the range of diffusivities among the many species in a reacting flow can result in the structure of the mixing field being quite different from predictions that apply the uniform diffusivity assumption. In Sec. III A, we examine the spatial structure of both the ξ and ξ fluctuation fields, and the changes in these fields due to changes in Reynolds number. Probability distributions of ξ are explored in Sec. III B. In Sec. III C we present power spectral densities determined from one-dimensional spatial profiles of the ξ fields. Power spectra of ξ (or similarly defined variables) are generally assumed to take on a much different form from spectra of conventional scalar variables,[12] owing to the presence of the source term in Eq. (3). Finally, we will investigate the structure of the differential diffusion by considering spatial auto-correlations through the ξ fields, as well as by examining the spatial distribution of layer structures in the dissipation field of ξ (Sec. III D).

II. EXPERIMENTAL ARRANGEMENT

A. Laser diagnostic method

This work employs Rayleigh scattering, which is the elastic scattering of light from molecules or small particles with characteristic size much smaller than the light wavelength,[22] to measure differential diffusion in a flow consisting of an initially mixed helium-propane jet issuing into a slow co-flow of air. The intensity of scattered light is proportional both to the intensity of the incident laser light and the Rayleigh scattering cross section of the medium. The Rayleigh scattering cross section of a given species i, i.e., σ_i, is related to its index of refraction n_i as $\sigma_i \sim (n_i - 1)^2$. The scattering cross section of a mixture is simply the mole fraction-weighted average of the constituent cross sections, or

$$\sigma_m = \sum_{i=1}^{N} X_i \sigma_i \sim \sum_{i=1}^{N} X_i (n_i - 1)^2, \tag{4}$$

where X_i is the mole fraction of species i, and N is the number of species in the mixture. In a two-component flow system, Rayleigh scattering directly yields the mole fractions of each species. Since differential diffusion is inherently a phenomenon involving three or more species, the interpretation of the Rayleigh scattering signal in this type of flow is not as simple. The method proposed by Bilger and Dibble, which is adapted here, relies on a precise composition of the initial jet mixture. The jet consists of two species, one (propane) with a refractive index that is greater than that of air, and one (helium) with a refractive index less than that of air. If the two gases are initially mixed such that the Rayleigh scattering cross section of the jet is the same as the scattering cross section of air, then any local change in the scattering signal is

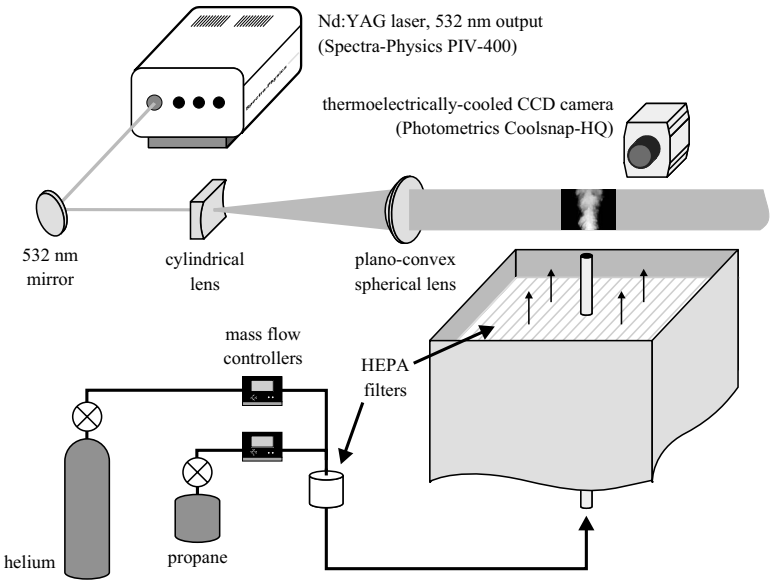

FIG. 1. A schematic depiction of the experimental arrangement. The light source is a dual-cavity Nd:YAG laser, and images are acquired with a thermoelectrically cooled CCD camera. The flow is a mixture of propane and helium that issues from a round pipe into a slow, filtered air co-flow.

directly indicative of departure of the helium-propane ratio from its initial value. By Eq. (4), and given the refractive indices of propane, helium, and air, which are, respectively, $n_{C_3H_8} \approx 1.001\,100$, $n_{He} \approx 1.000\,035$, and $n_{air} \approx 1.000\,290$ (Ref. 23), a mixture of 93.1% helium and 6.9% propane will have a nominal scattering cross section that is matched to the air value. The differential diffusion parameter ξ then relates to the scattering signal as

$$\xi = \frac{(\Pi - 1)\sigma_{air}}{(\sigma_{C_3H_8} - \sigma_{He})X^0_{C_3H_8}X^0_{He}}, \tag{5}$$

where Π is the intensity of scattered light, corrected for nonuniformities in the incident laser energy and in the imaging camera response, and normalized so that $\Pi = 1$ when the local scattering cross section is equal to that of air. The parameter ξ can be interpreted as the local excess (or deficit) of propane as compared with the expectation based on equal diffusivity with helium. In regions where ξ is positive, the propane-helium ratio is greater than at the jet exit, and where ξ is negative it is smaller. In regions where the propane-helium ratio is unchanged from the initial value, or in regions with no jet fluid present, $\xi = 0$.

B. Experimental conditions

The experimental arrangement is shown schematically in Fig. 1. The helium-propane mixture issues from a round pipe ($d = 4.6$ mm) into a slow, filtered air co-flow ($u_\infty \approx 0.5$ m/s). Filtering with a high-efficiency (HEPA) filter is necessary to eliminate any Mie scattering from particulates that could potentially overwhelm the Rayleigh scattering signal. The jet gas flow rates are measured and regulated by two Sierra Instruments C-100 mass flow controllers. Additional damping of high-frequency fluctuations in the flow rates is provided by including a large (length 1.2 m, inner diameter 0.05 m) pipe in the flow path. The light source is a dual-cavity Nd:YAG laser (Spectra-Physics PIV-400), capable of approximately 350 mJ per pulse at 532 nm. Both laser cavities are fired during each exposure, making the intensity of incident light approximately 700 mJ per image. The laser pulses pass through a sequence of sheet-forming optics that generates a laser sheet with a constant height of approximately 30 mm, and a thickness at the focal point (which is located within the imaging window) of approximately 200 μm. The Rayleigh scattering signal is captured by a thermoelectrically cooled CCD camera (Roper Scientific CoolSNAP HQ), with 1392×1040 pixel resolution. In these experiments, the camera is binned to 464×346 pixels to increase signal levels and reduce noise.

The experimental conditions for this paper are summarized in Table I. We consider four jet Reynolds numbers, namely, $Re_0 = 1000$, 1500, 2500, and 3000, where Re_0 is determined from the jet exit bulk velocity and the nozzle diameter (u_0 and d, respectively); the density of a 0.931/0.069 helium-propane mixture at 20 °C and atmospheric pressure ($\rho_m = 0.283$ kg/m^3); the dynamic viscosity of the mixture, i.e., 1.67×10^{-5} kg/m s (μ_m is itself found from the viscosities of helium and propane, 1.98×10^{-5} and 8.05×10^{-6} kg/m·s, respectively; and the formulas in Bird *et al.*[24]). The present measurements span between approximately $2d$ and $26d$ from the jet exit, in a series of five imaging windows (labeled "I" through "V"). In this relatively near-field region, the flow is generally not considered to have attained its asymptotic, self-similar state in terms of the statistics of turbulent scalar and velocity fluctuations (e.g., Dowling and Dimotakis[25]). This is nonetheless an interesting region in the context of nonpremixed combustion applications, where the details of the near-field mixing directly affect flame ignition, stability, and other issues. The imaging windows straddle the jet centerline in all cases, and extend up to $6.2d$ off the centerline in the radial direction.

We can assess the relative resolution of these measurements by comparing grid spacing of the measurements, i.e., Δx, with the local dissipation length scale λ_ν, as defined by Su and Clemens,[26] namely,

TABLE I. Run conditions and window parameters for the imaging experiments. Re_0 is the jet exit Reynolds number based on the mixture kinematic viscosity ($\nu_m = 5.9\times10^{-5}\ \mathrm{m}^2/\mathrm{s}$), nozzle diameter ($d = 4.6$ mm), and the jet exit bulk velocity (u_0). Re_δ is the outer-scale Reynolds number, estimated using the kinematic viscosity of air, and using standard scaling relations for the jet mean centerline velocity and the full width of the velocity profile. The successive window downstream locations are labeled "I" through "V." For each window, $x_{\min}$ and $x_{\max}$ are the upstream and downstream limits, respectively, of the measurement windows, while r_L and r_R represent the maximum radial displacement on either side of the jet centerline. The grid spacing in the windows is given by Δx. The parameter $\lambda_{\nu,\min}$ estimates the minimum dissipative length scale in each window.

Re_0	u_0	Re_δ	Window	$(x_{\min}, x_{\max})$	(r_L, r_R)	Δx, μm	$\lambda_{\nu,\min}$, μm
1000	13.0 m/s	4300	I	$(2.0d, 5.7d)$	$(1.9d, 3.0d)$	49	—
			II	$(7.0d, 10.5d)$	$(2.3d, 2.3d)$	46	220
			III	$(11.4d, 16.7d)$	$(3.8d, 3.5d)$	72	360
1500	19.3 m/s	6400	II	$(5.0d, 10.7d)$	$(5.8d, 1.8d)$	75	—
			III	$(10.0d, 15.7d)$	$(5.8d, 1.7d)$	75	230
			IV	$(15.0d, 20.7d)$	$(5.9d, 1.6d)$	75	350
			V	$(20.1d, 25.8d)$	$(6.2d, 1.3d)$	75	470
2500	32.6 m/s	9600	I	$(2.0d, 5.7d)$	$(1.9d, 3.0d)$	49	—
			III	$(10.9d, 16.5d)$	$(6.2d, 1.4d)$	75	190
			IV	$(15.7d, 21.3d)$	$(6.2d, 1.4d)$	75	270
3000	39.1 m/s	13 000	I	$(2.0d, 5.7d)$	$(1.9d, 3.0d)$	49	—
			III	$(10.9d, 16.5d)$	$(6.2d, 1.4d)$	75	150
			IV	$(15.7d, 21.3d)$	$(6.2d, 1.4d)$	75	210

$$\lambda_\nu(x) = \Lambda_\nu \delta(x) \mathrm{Re}_\delta^{-3/4}, \tag{6}$$

where δ is the full width of the velocity profile at 5% of the maximum (centerline) velocity, $u_c(x)$, $\mathrm{Re}_\delta \equiv u_c \delta / \nu_{\mathrm{air}}$ is the outer-scale Reynolds number (also shown in Table I), and Λ_ν is a proportionality constant whose value is of order 10. No velocity measurements are performed here, so we apply the recommended scalings for $u_c(x)$ and $\delta(x)$ given in Chen and Rodi,[27] assuming negligible buoyant acceleration:

$$u_c = 6.2 u_0 \sqrt{\frac{\rho_0}{\rho_\infty}} \left(\frac{x}{d}\right)^{-1}, \quad \delta = 0.36x. \tag{7}$$

For round jets Re_δ is constant, so the dissipation scale λ_ν increases with downstream distance. Accordingly, Table I gives λ_ν at the upstream limit of each of the measurement windows, where the demands on measurement resolution are most stringent. The measurement grid spacing Δx comfortably resolves λ_ν throughout the imaging region. (We do not quote λ_ν for window I because the flow has not necessarily undergone the turbulent transition there.)

It is customary to use the kinematic viscosity of air (here, $1.5\times10^{-5}\ \mathrm{m}^2/\mathrm{s}$) in the definition of Re_δ, under the assumption that the entrained ambient air quickly forms the preponderance of jet fluid. Ricou and Spalding[28] examined this by measuring mass entrainment rates for axisymmetric turbulent jets, and found that $m(x)$, the mean mass flow rate across fixed-x sections, is given by

$$\frac{m(x)}{m_0} = 0.32 \sqrt{\frac{\rho_\infty}{\rho_m}} \frac{x}{d}, \tag{8}$$

where m_0 is the jet exit mass flow rate. Here, $\rho_\infty/\rho_m = 4.3$, so the mean flow consists of 75% entrained fluid at $6d$ from the jet origin, and 90% entrained fluid at $15d$. Jet flows with significant density variation, such as this one, then have a significant disparity between the exit Reynolds number, which describes the initial jet development and turbulent transition, and the outer-scale Reynolds number, which describes the downstream turbulence level. In the present jets the jet exit Re_0 are moderate; as we shall see in Sec. III, the $\mathrm{Re}_0 = 1000$ and 1500 cases have lengthy laminar regions at the outset. The Re_δ values are comparatively high. Dimotakis[29] has argued that the asymptotic, high-Re state of turbulent mixing is realized beyond the so-called mixing transition. That paper identified the critical outer-scale Reynolds number (which, for jets, was defined similarly to the present Re_δ, in terms of the mean centerline velocity and jet full-width) for the mixing transition as being in the range 10 000–20 000. The $\mathrm{Re}_0 = 3000$ jet here has $\mathrm{Re}_\delta = 13\,000$, and thus is in the range where we expect the mixing transition to occur. The results from the downstream windows in the $\mathrm{Re}_0 = 3000$ case should, therefore, be fairly representative of high-Re turbulent mixing.

C. Data reduction

For determining the variable ξ from the Rayleigh scattering images, the data reduction procedure accounts for the

background light levels, spatial nonuniformity in the camera array response, and spatial variations in the incident laser sheet energy, through a three-step procedure. The accuracy of these corrections is especially important in view of the relatively low signal levels in these scattering experiments. A common method to determine the magnitude of the nonzero camera offset, as well as any unwanted reflections that may reach the camera lens, is to block off the light source and record images of the dark "background" seen by the imaging system. We have found that this method does not accurately reproduce the background light that is seen during data collection, because many of the uncontrolled reflections that result as the laser sheet passes through the imaging facility are lost. Instead, we implement a procedure where only a portion ($\approx$5 mm) of the $\approx$30 mm high laser sheet is blocked off just prior to entering the imaging region. The background signal levels in the "shadow" of the beam block then appropriately include the effects of the passage of the sheet through the facility. We can construct a full background correction field by traversing the beam block incrementally across the laser sheet, then concatenating the shadow regions from the resulting images. From separate scattering experiments performed using the same facility,[30] it was found that this method significantly improves the imaging accuracy, particularly in regions of moderate incident laser intensity.

Subsequent to the background subtraction step, the data reduction procedure accounts for nonuniformity in the laser sheet intensity and in the camera response. Scattering images collected in the measurement region with purely ambient air present correspond to a uniform scattering cross section, so by dividing these images (appropriately background-subtracted) from the background-subtracted jet images, we correct for the spatial variations in the laser sheet intensity, including sheet attenuation in the propagation direction, and camera response non-uniformities in an averaged sense. However, the laser sheet intensity, and its cross-sheet intensity profile, can vary noticeably from pulse to pulse, so we correct for these effects on an instantaneous basis, in the final step of the data reduction. In each jet imaging window, we ensure that a region of pure ambient air is visible everywhere along one side of the jet. Again, signal variations along that side of the image will be due solely to variations in laser sheet intensity, and by incorporating information on the sheet propagation geometry, we can create an instantaneous correction image that accurately represents the intensity profile for a given laser pulse. Upon applying this correction to obtain the fully processed intensity field Π, we determine the ξ field through the application of Eq. (5).

D. Flow system calibration and measurement uncertainty

As emphasized by Dibble and Long,[7] precise control of the proportion of helium and propane in the initial jet mixture is critical to successful application of this experimental arrangement. Specifically, the interpretation of the Rayleigh scattering signal as proportional to the differential diffusion parameter ξ requires precise matching of the Rayleigh scattering cross section of the jet mixture to the cross section of air. Owing to impurities in the jet gases and the inaccuracies of commercial flowmeters, we undertake calibration tests for each gas sample, and at flow rates characteristic of the experimental conditions, to determine the helium-propane ratio that appropriately matches the scattering cross sections of the jet fluid and air. These calibration tests involve the Rayleigh scattering imaging of the potential core of a laminar jet, for different helium-propane ratios in the neighborhood of the theoretical 0.931/0.069 value. To obtain an extended laminar flow region, and thus a larger potential core, for the given flow rates, we reduce the jet Reynolds number by replacing the standard 4.6 mm nozzle with a 10.0 mm nozzle. Figure 2 illustrates the calibration process. Figure 2(a) shows a representative averaged ξ field for a jet mixture with an indicated helium mole fraction of $X^0_{\mathrm{He}}=0.9367$. The volumetric jet flow rate was $5.51\cdot10^{-4}$ m^3/s, giving a jet Reynolds number of 1200 with the large nozzle. The averaging includes 500 planes in each case, and the scattering images are fully corrected according to the procedure described in Sec. II C. Figure 2(b) shows the radial profiles of ξ for initial helium mole fractions varying from $X^0_{\mathrm{He}}=0.9357$ to 0.9386, compiled at $x/d=2.5\pm0.3$. The uniform composition of the core region is evident in the profiles. If the scattering cross section of the jet mixture is perfectly matched to the air value, then ξ will equal zero in the jet core. The ξ value in the jet core varies approximately linearly for small variations in X^0_{He}, as shown in Fig. 2(c), so the indicated helium-propane ratio that allows the scattering cross section of the jet fluid to match that of air is found easily through linear interpolation. For this particular calibration, the proper jet mixture consists of 93.63% helium and 6.37% propane, as indicated by the mass flow controllers. Because the experiment does not rely on the mass flow calibrations provided by the flowmeter manufacturer, the experimental error is described here by the repeatability of the flow controllers (nominally 0.2%) rather than by their calibration accuracy (nominally 1.0%).

We are particularly concerned with the effects of measurement uncertainties on the imaging results, because of the very low signal levels that characterize these experiments. The effective signal-to-noise ratio (SNR) varies throughout the imaging region due to the uneven distribution of incident laser light. Prior to the data reduction, each image is cropped to eliminate those rows on the top and bottom in which the incident light intensity is particularly low. The SNR computed from the processed, cropped images varies from approximately 70 in the central rows of the images, where the incident light intensity is highest, to 50 in the extreme rows. Most of the analysis (the exception is the analysis of layer thicknesses in Sec. III D) in this paper employs ξ fields that have been passed through a 3×3 median filter. Postfiltering, the SNR varies from approximately 120 to 150.

A source of error unique to this experiment concerns the possible deviation of the helium and propane mole fractions from their calibrated values. In the data reduction process, interpretation of the variable ξ as proportional to the adjusted flat-field corrected image intensity $(\Pi-1)$ relies on the assumption that the scattering cross section of the jet mixture is matched to the air value; i.e., that $\sigma_{\mathrm{air}}=X^0_{\mathrm{C_3H_8}}\sigma_{\mathrm{C_3H_8}}+X^0_{\mathrm{He}}\sigma_{\mathrm{He}}$.

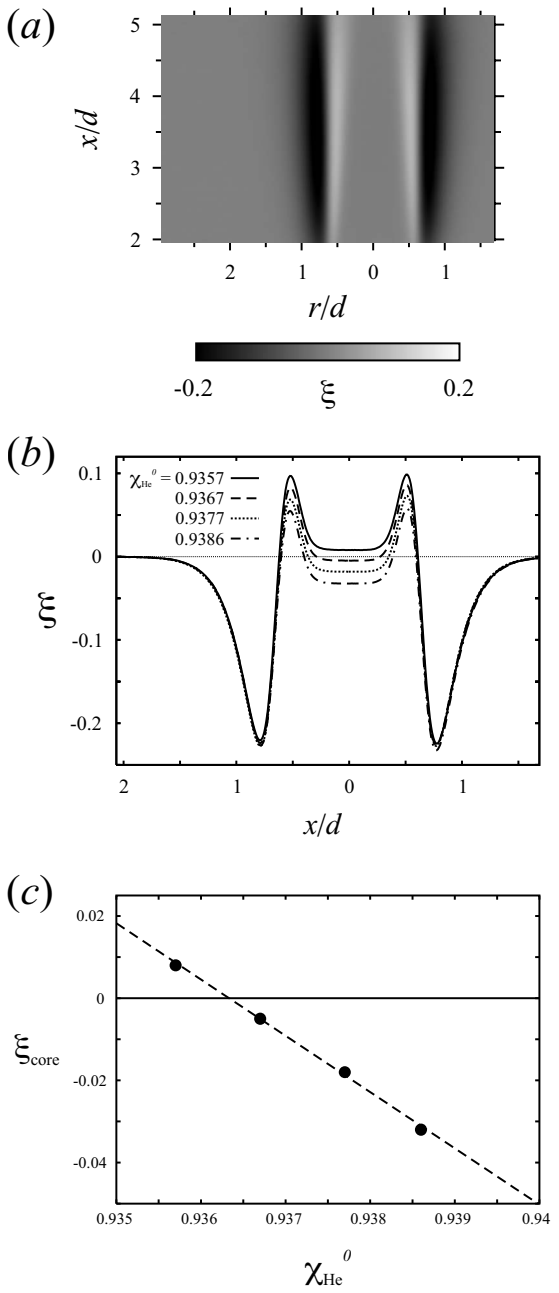

FIG. 2. (a) A sample averaged scattering ξ field from the mole fraction calibration process, with jet diameter 10 mm and $\mathrm{Re}_0=1200$. For this case the indicated helium mole fraction in the jet mixture was $X^0_{\mathrm{He}}=0.9367$. (b) Profiles of the computed ξ value, for X^0_{He} values between 0.9357 and 0.9386, compiled at $x/d=2.5\pm0.3$. (c) The ξ value in the jet core for the different X^0_{He} values. The least-squares fit shown gives $\xi=0$ for an indicated $X^0_{\mathrm{He}}=0.9363$.

To determine the effect of miscalibration in the initial jet mixture fraction, we define an uncertainty variable ϵ as

$$\epsilon \equiv X^0_{\mathrm{C_3H_8}}\sigma_{\mathrm{C_3H_8}} + X^0_{\mathrm{He}}\sigma_{\mathrm{He}} - \sigma_{\mathrm{air}}. \tag{9}$$

The expression for ξ as a function of the processed image intensity, for the case of nonzero ϵ, is, then,

$$\xi = \frac{(\Pi-1)\sigma_{\mathrm{air}}}{(\sigma_{\mathrm{C_3H_8}}-\sigma_{\mathrm{He}})X^0_{\mathrm{C_3H_8}}X^0_{\mathrm{He}}} + \frac{\epsilon(1-X_{\mathrm{air}})}{(\sigma_{\mathrm{C_3H_8}}-\sigma_{\mathrm{He}})X^0_{\mathrm{C_3H_8}}X^0_{\mathrm{He}}}$$
$$= \frac{(\Pi-1)\sigma_{\mathrm{air}}}{(\sigma_{\mathrm{C_3H_8}}-\sigma_{\mathrm{He}})X^0_{\mathrm{C_3H_8}}X^0_{\mathrm{He}}} + \delta\xi. \tag{10}$$

Thus, if we determine ξ using Eq. (5) in a case where the jet mixture calibration is incorrect, the term $\delta\xi$ in Eq. (10) describes the resulting error in ξ. In these experiments, where the initial mole fractions are nominally $X^0_{\mathrm{He}}=0.931$ and $X^0_{\mathrm{C_3H_8}}=0.069$, an uncertainty of 0.2% in the flowmeter repeatability corresponds to an uncertainty in the initial jet constituent mole fractions of 0.0019, with the result that

$$\delta\xi \approx 0.0296(1-X_{\mathrm{air}}). \tag{11}$$

The uncertainties in the measured ξ thus depend directly on the local mole fraction of air; i.e., the degree to which the jet has mixed with the surrounding fluid. In the jet core, where $X_{\mathrm{air}}=0$, $\delta\xi\approx0.0296$. At $x=20d$, near the downstream limit of the measurement region, standard estimates of jet concentration scaling[27] suggest that averaged jet fluid mole fractions will have maximum values on the order of 0.2, corresponding to $\delta\xi\approx0.0059$.

III. RESULTS

Figure 3 shows sample instantaneous ξ fields for $\mathrm{Re}_0=1000$, 2500, and 3000. The jet fluid is predominantly helium, so buoyancy has a minor effect on the evolution of the mean velocity, resulting in a local Reynolds number that increases slightly with downstream distance. The $\mathrm{Re}_0=1000$ jet (Fig. 3(a)) is initially laminar, as is evident in the upstream imaging window. In a laminar jet with differential diffusion, there is a clear large-scale structure to the mixing field. The outermost contour exhibits an excess of the more diffusive fluid (negative ξ), while the center of the jet, near the nozzle, is undisturbed ($\xi=0$). In between, there is a region of positive ξ, or an excess of the less diffusive fluid, due to the rapid radial movement of the more diffusive fluid. The $\mathrm{Re}_0=1000$ jet generally undergoes the turbulent transition between $x/d=6$ and 8. It is reasonable to surmise that the properties of the ξ field downstream of the transition point depend strongly on the structures that develop in the laminar region. For example, ξ structures observed in the turbulent part of the flow may have formed in the laminar region, then simply advected through the turbulent region.

The ξ fields for the $\mathrm{Re}_0=2500$ and 3000 jets are shown in Figs. 3(b) and 3(c), respectively. It is clear from the upstream imaging windows that the jets at these Reynolds numbers become turbulent much more quickly than the $\mathrm{Re}_0=1000$ jet. Owing to the rapid jet spread in these cases, and also in order to maintain a good level of resolution, the downstream imaging windows span half of the jet only. The $\mathrm{Re}_0=2500$ flow shows a more pronounced potential core than the $\mathrm{Re}_0=3000$ flow, and there is evidence at the upstream side of the measurement domain ($x/d\approx2$) that the characteristic laminar ξ structure was present near the nozzle exit, while for $\mathrm{Re}_0=3000$, there is only a very small trace of any laminar-like structure such as that seen at $\mathrm{Re}_0=1000$.

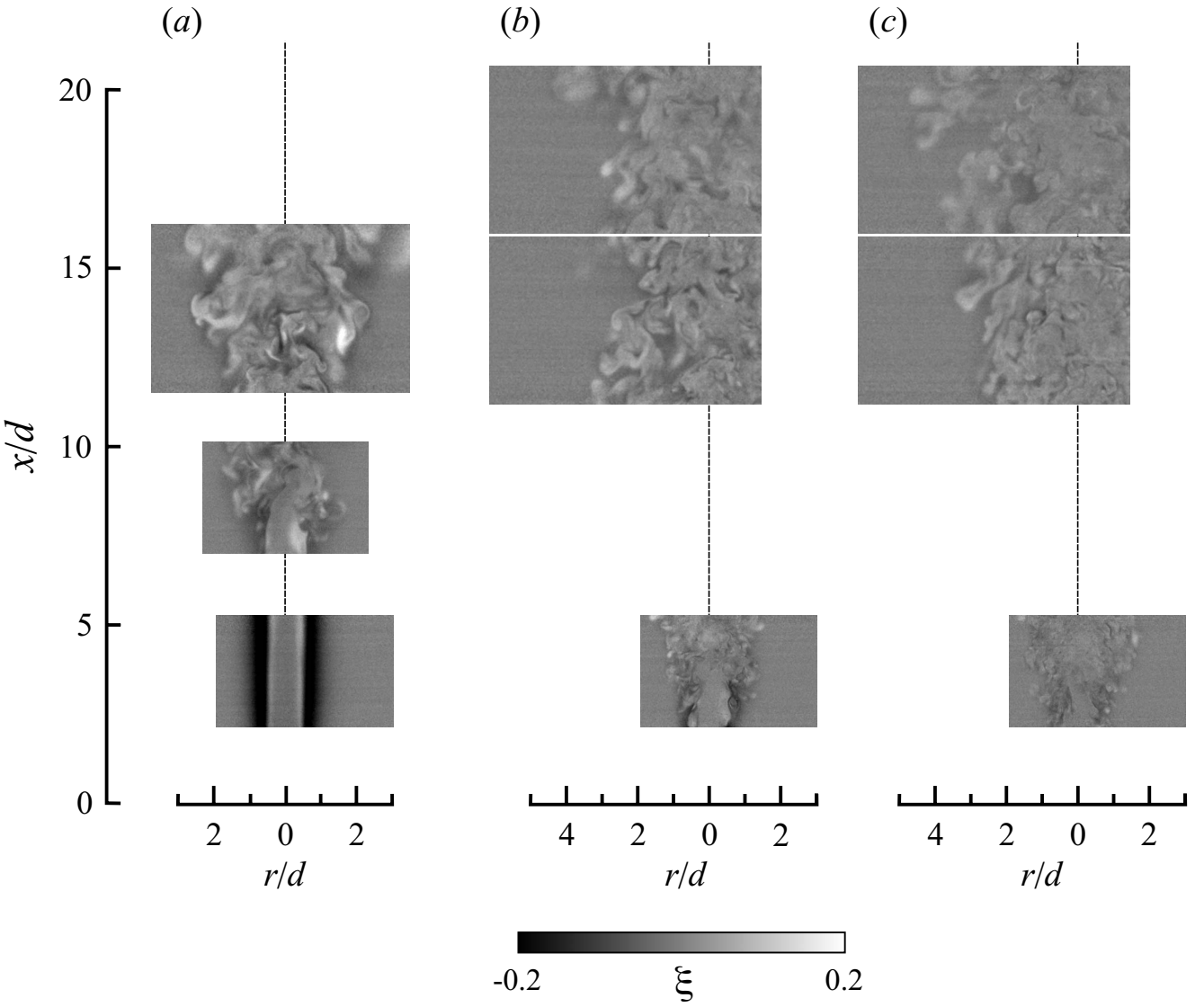

FIG. 3. Sample instantaneous ξ fields from the jets with exit Reynolds number (a) 1000, (b) 2500, and (c) 3000. The $Re_0=1000$ jet is clearly laminar throughout the upstream imaging window, so many of the visible differential diffusion structures in the downstream windows would have formed in the near-nozzle laminar flow regions. The laminar regions manifest a clear tendency for the highly diffusive helium to diffuse preferentially to the outer boundary of the jet (giving $\xi<0$), leaving a thin zone characterized by excess propane ($\xi>0$) to the inside. At $Re_0=3000$ the jet, in contrast, is essentially turbulent from the outset, so the ξ structures develop in an underlying turbulent flow.

We can compare the relative turbulence levels of the $Re_0=1000$, 2500, and 3000 cases in the near field by considering mean radial profiles of ξ and the root-mean-square ξ fluctuations, as compiled in Fig. 4 for $x/d=2.25\pm0.11$. Consistent with the instantaneous fields in Fig. 3, the mean ξ profiles in Fig. 4(a) show that the characteristic laminar structure is very evident for $Re_0=1000$, somewhat evident at $Re_0=2500$, and basically not evident at $Re_0=3000$. The profiles of ξ'_{rms} (Fig. 4(b)) show a bimodal structure for all cases, with the peak fluctuations being located in the initial jet shear layer. For the $Re_0=1000$ case the flow is laminar at the profile location, so the fluctuations in ξ are much smaller than the mean ξ magnitudes, and arise from minor unsteadiness in the jet trajectory. The differences in the two higher Re_0 cases are particularly instructive. The ξ'_{rms} values at $Re_0=2500$ are relatively high, consistent with notable turbulence levels; however, the peak mean ξ magnitudes are larger than the peak ξ'_{rms}, indicating that the structure, and thus the laminar origins, of the mean ξ field also predominate in the instantaneous fields. In this sense, the $Re_0=2500$ case is transitional at the profile location. In contrast, the peak ξ'_{rms} values for the $Re_0=3000$ case are larger than the peak mean ξ values, indicating that turbulence is the dominant factor in establishing the instantaneous ξ fields. The increased turbulence at $Re_0=3000$ versus 2500 is also seen in the slightly wider fluctuation peaks at the higher Reynolds number. In the absence of measurements immediately downstream of the jet exit (which are precluded in this imaging method by reflections from the jet nozzle), it seems safe to argue that the $Re_0=3000$ case is essentially turbulent from the outset.

In the downstream imaging windows, differential diffusion is seen in the ξ fields for both of the higher Reynolds

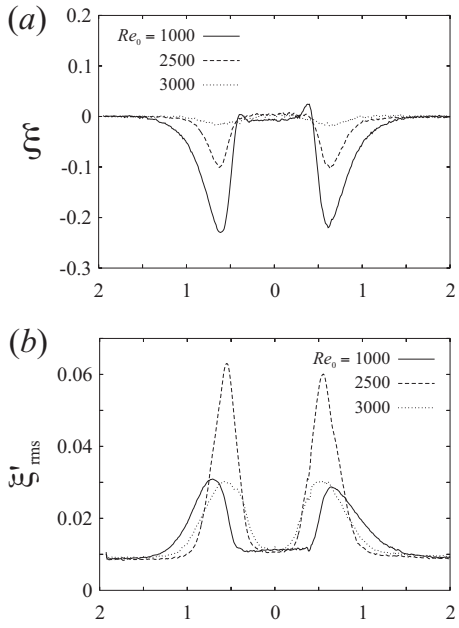

FIG. 4. Radial profiles of (a) the mean ξ and (b) the root-mean-square ξ fluctuations, compiled at $x/d=2.25\pm0.11$ for $\mathrm{Re}_0=1000$, 2500, and 3000. The profiles for $\mathrm{Re}_0=1000$ show clearly the characteristic laminar structure of ξ, while the $\mathrm{Re}_0=3000$ profiles are consistent with a mixing field that is essentially turbulent from the outset.

numbers in Fig. 3. The peak ξ values are of comparable magnitude for the two Reynolds numbers, though by inspection the characteristic sizes of the ξ structures are smaller for the $\mathrm{Re}_0=3000$ case. From the evidence of the upstream measurement windows, we would expect that the differential diffusion that is seen downstream in the $\mathrm{Re}_0=2500$ and 3000 flows may have different origins than that observed in the $\mathrm{Re}_0=1000$ jet. In particular, the ξ structures for the higher Reynolds numbers will generally have formed in flow regions characterized by at least moderate turbulence. We will explore the differences in the ξ fields that result from laminar and turbulent underlying velocity fields in subsequent sections.

A. Evolution of the mean and fluctuating ξ fields

The mean ξ field for the $\mathrm{Re}_0=1500$ jet is shown in a series of four imaging windows in Fig. 5(a). The jet has an extended laminar region, as with the $\mathrm{Re}_0=1000$ jet in Fig. 3(a), and becomes turbulent in the range $x/d=6-8$. Figure 5(b) shows radial profiles of the mean ξ fields, for $x/d=6$, 7, 9, 13, and 23. The laminar differential diffusion structure described earlier is evident in the two transitional profiles ($x/d=6$ and 7), though there is a clear de-emphasis of the characteristic ξ peaks in the $x/d=7$ profile. In the turbulent region, the mean ξ values rapidly approach zero as the proportion of ambient fluid increases due to entrainment.

However, while the ξ magnitudes diminish in the turbulent region, structural organization persists. Figure 6 shows radial profiles of mean ξ for $x/d=13$, 17, and 23, rescaled relative to those in Fig. 5(b) to emphasize the small magnitudes. These profiles in the turbulent region reveal a noticeable tendency for propane to be in excess on the outer boundary of the jet, and for helium to be in excess at the center of the jet, in a reversal of the laminar trend. This reversal was also previously observed by Kerstein *et al.*[6] It is clear that this turbulent profile shape is not a purely diffusive phenomenon, since the diffusive mechanism results in profiles of the form of those at $x/d=6$ and 7 (Fig. 5(b)), where zones of excess helium surround zones of excess propane. Instead, the presence of regions of excess propane on the jet boundary arises through the combined effects of molecular diffusion and turbulent advection. Differential diffusion first generates regions of nonzero ξ from the original $\xi=0$ jet, then turbulent advection distributes the resulting ξ structures (turbulence alone, of course, cannot generate $\xi\neq0$ regions). We would expect that the low Re flows would show this turbulent ξ profile more strongly than the higher Re flows, owing to the significant $\xi\neq0$ structures that develop in the near-nozzle laminar region. This is borne out by the experiments, although the $\mathrm{Re}_0=2500$ and 3000 cases do show a continued excess of propane to the outside of the jet, and helium to the inside, which confirms that the form of the ξ profile in the turbulent region develops independently of the original process by which the $\xi\neq0$ structures arise.

We hypothesize that there are two likely mechanisms for the excess of propane on the jet boundary, relating, respectively, to inertial and gravitational effects. In the inertial mechanism, the higher mass of fluid particles containing excess propane ($\xi>0$) means that when those particles are subjected to turbulent fluctuations in the positive-r direction, they are more likely to reach the boundary of the jet than when lighter fluid particles with excess helium ($\xi<0$) are subjected to similar velocity fluctuations. These radially outward fluctuations might relate, for example, to large-scale swirling motions in the jet, in which case the inertial mechanism describes a centrifugal separation of the propane and helium, akin to cyclonic separation techniques. The gravitational mechanism, in contrast, is posited on the disparate buoyant acceleration encountered by fluid particles with excess propane or helium. The downstream component of the instantaneous velocity vector is likely to be larger for $\xi<0$ particles, which may cause $\xi>0$ particles to be pushed toward the boundary of the jet. However, determining the relative importance of these mechanisms would require simultaneous velocity field measurements, which are not part of the present study.

The values of the mean ξ variable used to quantify the differential diffusion become very small with increasing distance from the jet exit, so it is instructive to consider the magnitudes of the ξ fluctuations. Figure 7 shows the rms ξ-fluctuation fields for $\mathrm{Re}_0=1000$, 2500, and 3000, in the same imaging windows previously shown in Fig. 3. For each of the images, the mean ξ fluctuation levels in the ambient region, which result from noise in the measurement and data reduction procedure, have been subtracted. The ξ'_{rms} images show a clear bimodal form, with the peak values being found near the edge of the jet, which is also familiar from conventional scalar fluctuation measurements in jets.[25] However, the interpretation of ξ'_{rms} in these measurements is not wholly analogous to the interpretation of conventional scalar fluctuation fields. Conventional scalar fluctuations arise through

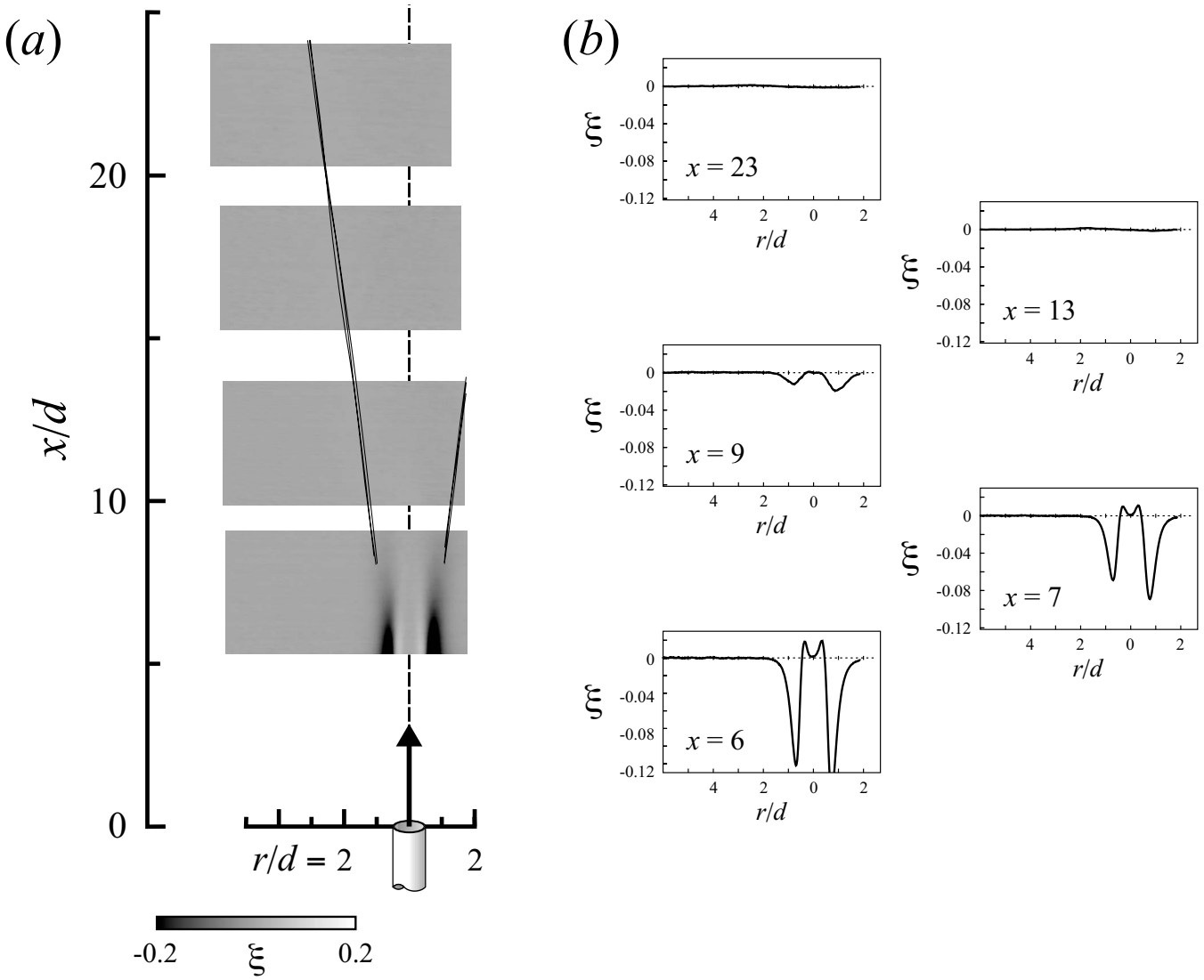

FIG. 5. Mean ξ fields (a) and corresponding radial profiles (b) for the $Re_0=1500$ jet. The characteristic laminar structure of the ξ field is evident through the transitional region. The ξ values rapidly approach zero in the turbulent region of the flow.

the advection of the scalar quantity by the turbulent flow field. The ξ fluctuations, on the other hand, can be generated both by the turbulent advection and by local differential diffusion. The broad similarity in the profile shapes between the ξ fluctuations and the conventional scalar fluctuations suggests that the turbulent mixing of the ξ field is decoupled from the generation of $\xi \neq 0$ structures (as also discussed in Sec. III A), particularly in that the downstream ξ'_{rms} profiles are not noticeably affected by the near-nozzle form of the mean ξ profiles.

The dependences of the fluctuation magnitudes on Reynolds number and axial position are explored in Fig. 8. Figure 8(a) compares the radial profiles of ξ'_{rms} at $x/d=13$ for Reynolds numbers $Re_0=1000$, 2500, and 3000, while

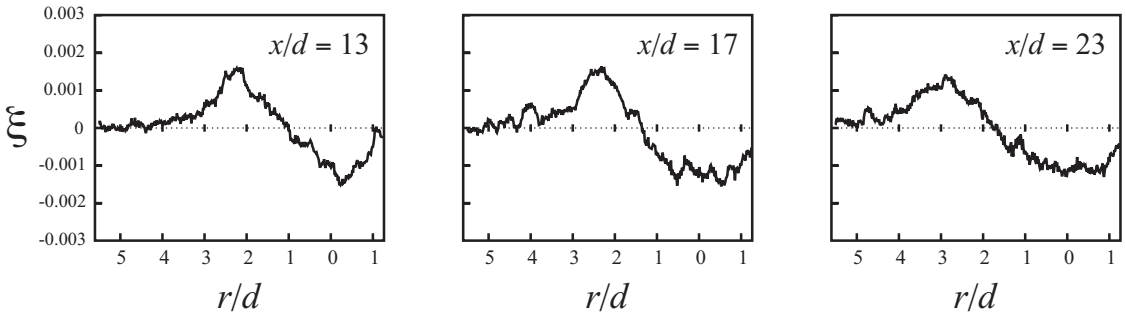

FIG. 6. Radial profiles of mean ξ for $x/d=13$, 17, and 23 in the $Re_0=1500$ jet, rescaled to show the persistence of the structural organization.

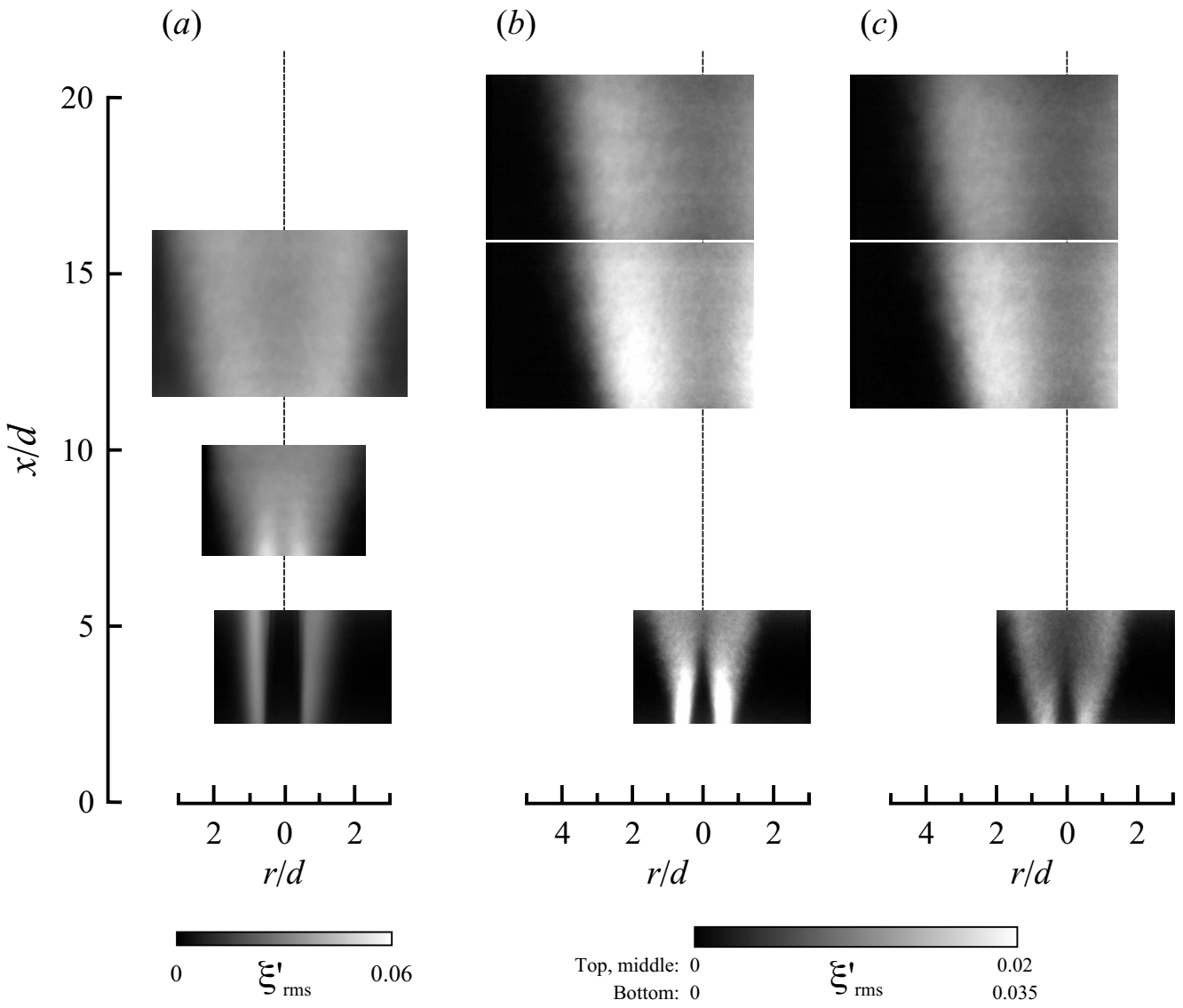

FIG. 7. Root-mean-square ξ fluctuation fields for jet exit Reynolds numbers (a) 1000, (b) 2500, and (c) 3000, for the same imaging windows shown in Fig. 3. The ξ'_{rms} field has a clear bimodal form for each Re_0, and at all downstream positions. The upstream imaging windows show the reduction in the potential core length with increasing Re_0.

Fig. 8(b) shows the profiles at $x/d=13$, 15, and 17 for $Re_0=2500$. The profiles are plotted in terms of the similarity coordinate x/δ', where δ' is defined as the radial position of the peak ξ'_{rms} value for a given profile. Kerstein *et al.*[12] applied a spectral analysis to predict a weak $Re^{-1/4}$ dependence of the peak ξ'_{rms} values. The profiles in Fig. 8 suggest that the disparity in peak ξ'_{rms} between the $Re_0=1000$ and 2500 cases exceeds a $Re^{-1/4}$ dependence. This is likely due to the significant nonzero ξ regions that develop in the laminar portion of the $Re_0=1000$ jet. The observed ξ fluctuations beyond $Re_0=2500$ do show the predicted weaker dependence on Re, although the current measurements do not span a sufficient Reynolds number range to allow determination of the specific functional dependence on Re_0.

Figure 9 shows the ξ'_{rms} profiles for $Re_0=1000$ and 2500, normalized by their individual maxima $\xi'_{rms,max}$. For the $Re_0=1000$ jet, the profile at $x/d=8$, in the transitional region, differs significantly from the post-transition profiles at $x/d=13$ and 15 (Fig. 9(a)). The $x/d=8$ profile has a much less pronounced bimodal form, even though the upstream laminar profiles are purely bimodal (Fig. 7(a)), with $\xi' \neq 0$ regions surrounding a $\xi' \approx 0$ core. The profiles at $x/d=13$ and 15 appear to be essentially self-similar. For the $Re_0=2500$ case, the profiles at the three locations shown in Fig. 9(b), i.e., $x/d=13$, 15, and 19, are also self-similar, though the self-similar profile differs from that for $Re_0=1000$; for example, the discrepancy between the peak ξ' value and that on the centerline is larger for the higher Reynolds number. It has also been observed in the mixing of conventional scalar quantities that self-similar profiles of the scalar fluctuations may depend on Reynolds number even when the self-similar profiles of the scalars themselves do not.[25] We also emphasize here that while Reynolds number variations do affect the ξ fluctuations, the characteristic form

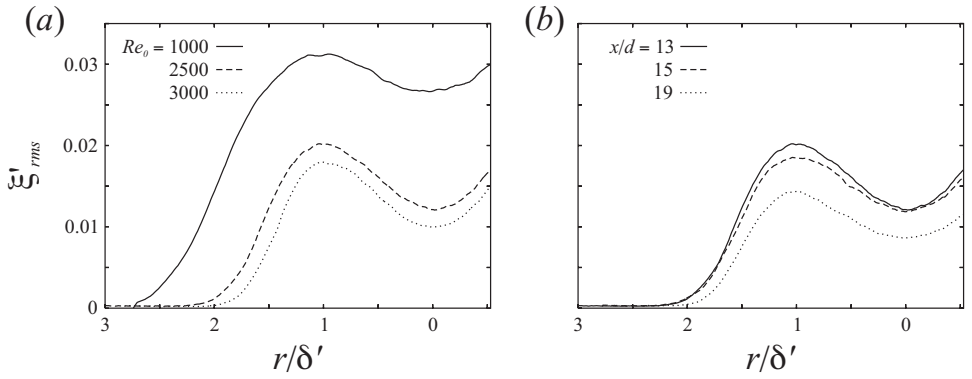

FIG. 8. Radial profiles of $\xi'_{\rm rms}$, (a) for $\mathrm{Re}_0=1000$, 2500, and 3000 at fixed $x/d=13$ and (b) at $x/d=13$, 15, and 17 for fixed $\mathrm{Re}_0=2500$, using a similarity form for the radial coordinate. The quantity δ' is defined as the radial position of the peak $\xi'_{\rm rms}$ value for a given profile. The wide disparity in peak $\xi'_{\rm rms}$ levels between $\mathrm{Re}_0=1000$ and the 2500 and 3000 cases is likely due to the lengthy laminar region seen for $\mathrm{Re}_0=1000$.

of the mean ξ profiles, with $\xi>0$ on the jet boundary and $\xi<0$ on the interior, appears to be a general property of the jet mixing.

The persistence of the differential diffusion that apparently arises in the laminar region of the $\mathrm{Re}_0=1000$ jet has important implications for practical flow systems. This is particularly true if the turbulence is highly intermittent. In combustion systems, local turbulence levels can be sharply reduced through heat release; gas densities have a nominal inverse dependence on temperature, i.e., $\rho\propto T^{-1}$, while dynamic viscosities vary approximately as $\nu\propto T^{0.7}$, so kinematic viscosity varies as $\nu\propto T^{1.7}$. In typical hydrocarbon flames, peak local temperatures can be over seven times the minimum temperatures, so local Reynolds numbers can vary by a factor of 30, and significant local laminarization may result. Even when the global flow Reynolds number is high, then, there may be sizable laminar regions in which differential diffusion develops and subsequently affects the downstream regions of the flow.

B. Probability distributions of ξ

Figure 10 shows probability distributions of ξ, for Reynolds numbers $\mathrm{Re}_0=1000$, 2500, and 3000. Compilation subwindows for the probability density functions (pdfs) are centered at axial positions $x/d=13$ and 19, and radial locations $r=0$, δ', and $2\delta'$, where δ' is, as above, defined as the distance between the centerline and the position of maximum $\xi'_{\rm rms}$. The subwindows span $0.65d$ in the x and r directions. Table II gives the mean ($\bar{\xi}$), root-mean-square fluctuations ($\xi'_{\rm rms}$), and skewness (γ) for the ξ distributions in Fig. 10.

The ξ pdfs for the $\mathrm{Re}_0=1000$ jet (Fig. 10(a)) at $x/d=8$ reveal clearly the transitional character of the flow. The ξ values on the centerline have a mean positive value, reflecting excess propane, while the ξ values on the outside of the jet ($r/\delta'=2$) have a mean negative value, reflecting excess helium. This is consistent with the form of the ξ fields in the near-nozzle, laminar region, as explored above (Sec. III A). However, the onset of turbulence is also clear in the relatively wide spread of the pdfs. For example, while the mean (and mode) of the ξ pdf at $r/\delta'=2$ is negative, there is a long tail to the positive side that results in a strong positive skewness, indicating that significant stirring of the laminar ξ field has taken place. The breadth of the $r/\delta'=2$ distribution also indicates that the turbulent activity extends well to the outside of the peak $\xi'_{\rm rms}$ location ($r=\delta'$). At $x/d=13$ in the $\mathrm{Re}_0=1000$ jet, the amount of turbulent mixing outside of $r=\delta'$ is lower, as embodied in the much narrower ξ pdf for $r/\delta'=2$. That pdf also shows a very high positive skewness,

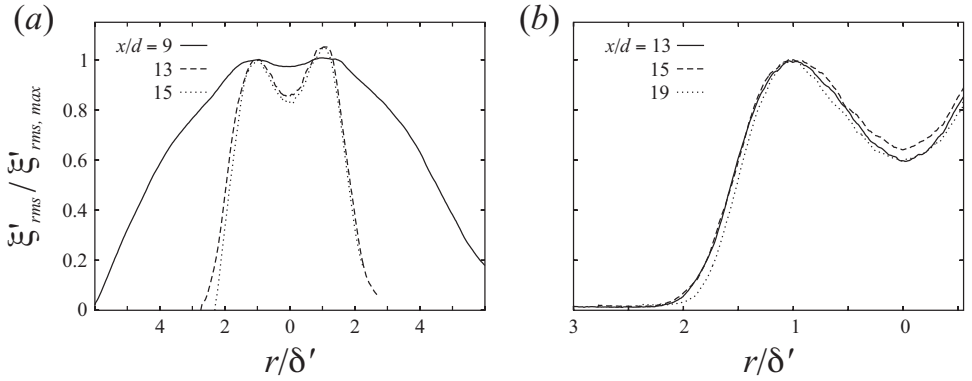

FIG. 9. Radial profiles of $\xi'_{\rm rms}$ for (a) $\mathrm{Re}_0=1000$ and (b) $\mathrm{Re}_0=2500$, in full similarity form. Each profile is normalized by its peak value $\xi'_{\rm rms,max}$. For $\mathrm{Re}_0=1000$ the profiles are located at $x/d=9$, 13, and 15, and for $\mathrm{Re}_0=2500$ the profiles are at $x/d=13$, 15, and 19. Save for $x/d=9$ at $\mathrm{Re}_0=1000$, which is in the transitional region, the profiles are nearly self-similar for each Reynolds number, though the profiles for different Re are not similar to each other.

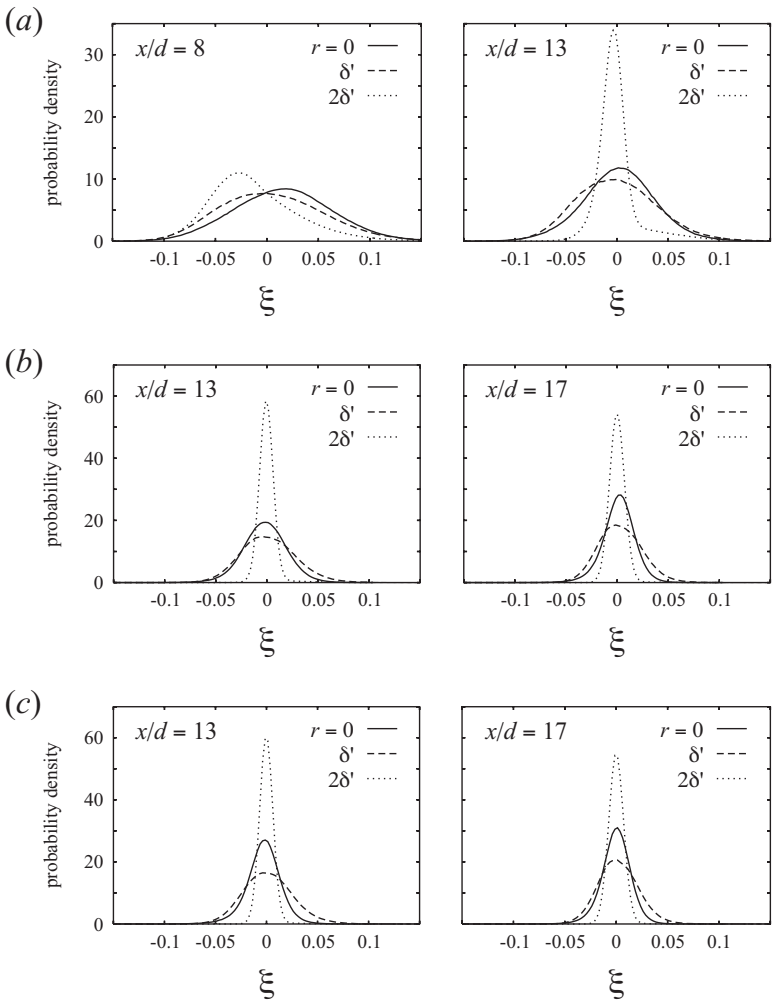

FIG. 10. Pdfs of ξ from (a) $\mathrm{Re}_0=1000$, (b) $\mathrm{Re}_0=2500$, and (c) $\mathrm{Re}_0=3000$ cases, for axial positions $x/d=13$ and 19, and for different radial locations within the jet. The pdfs are compiled in subwindows that span $0.65d$ in the x and r directions. The length scale δ' is the radial position of the peak values in the local ξ'_{rms} profile.

consistent with the intermittent presence of fluid elements containing excess propane. This suggests that the turbulent form of the mean ξ profiles (Fig. 6), in which $\xi>0$ toward the jet boundary, arises from relatively infrequent fluid elements with large ξ values.

The ξ pdfs for the $\mathrm{Re}_0=2500$ and 3000 jets (Figs. 10(b) and 10(c)) show a consistent form. The pdfs at all three radial locations have similar mode (which is very near $\xi=0$); the on-centerline and $r/\delta'=1$ pdfs also have similar variances, with the variance for the $r/\delta'=2$ pdf being considerably smaller. (As with the $\mathrm{Re}_0=1000$ jet at $x/d=13$, there is relatively little turbulent mixing outside of $r=\delta'$.) The on-centerline and $r/\delta'=1$ pdfs differ in their asymmetry: the $r/\delta'=0$ pdfs have negative skewness and the $r/\delta'=1$ pdfs have positive skewness. This, again, indicates that the characteristic turbulent ξ profile, with $\xi<0$ near the centerline

TABLE II. Statistical quantities determined from the ξ pdfs in Fig. 10: mean $\bar{\xi}$, rms fluctuations ξ'_{rms}, and skewness γ.

Re_0	r/δ'	x/d	$\bar{\xi}$	ξ'_{rms}	γ	x/d	$\bar{\xi}$	ξ'_{rms}	γ
	0		0.0166	0.0473	0.0682		0.0021	0.0361	0.0242
1000	1	8	0.0059	0.0508	0.2828	13	−0.0002	0.0401	0.3446
	2		−0.0144	0.0424	0.7026		−0.0001	0.0226	2.1735
	0		−0.0020	0.0221	−0.3069		0.0014	0.0161	−0.5306
2500	1	13	0.0016	0.0271	0.2684	17	0.0031	0.0215	0.1457
	2		0.0000	0.0090	1.8392		0.0001	0.0082	−0.5922
	0		−0.0029	0.0172	−0.0404		−0.0002	0.0143	−0.2852
3000	1	13	0.0015	0.0246	0.2856	17	0.0021	0.0196	0.2256
	2		0.0000	0.0074	1.3845		0.0001	0.0076	0.4087

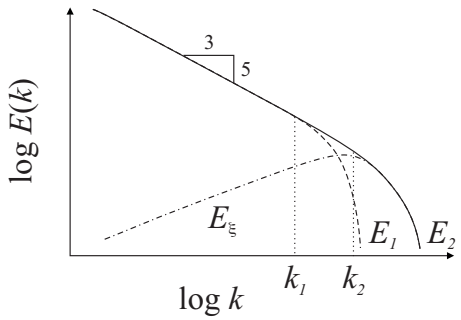

FIG. 11. Presumed form of E_ξ, the spectrum of ξ, following Kerstein *et al.* E_1 and E_2 are the spectra of more- and less-diffusive scalars, respectively. The Reynolds number is assumed to be sufficiently high that both scalars have a $k^{-5/3}$ inertial range. The wavenumbers k_i represent the diffusive cutoff length scales. The presumed E_ξ spectrum has a peak between the k_i.

and $\xi > 0$ toward the jet boundary, results from the intermittent presence of fluid particles whose propane-to-helium ratio departs noticeably from the initial value; i.e., where ξ is significantly different from zero.

The properties of the turbulent ξ pdfs thus argue that the turbulent ξ profile is more likely to arise from the inertial mechanism proposed in Sec. III A than from the gravitational mechanism. The inertial mechanism fundamentally relies on the action of turbulent radial velocity fluctuations. This is consistent with the explanation that intermittent events account for the disparities in the ξ pdfs at $r/\delta' = 0$ and $r/\delta' = 1$, by affecting the population of the tails of the pdfs. In contrast, the gravitational mechanism is ultimately founded on the lower average density of the jet fluid relative to the ambient air, and as a result is less dependent on the details of the turbulent fluctuations. If the form of the turbulent ξ were to be attributable to the gravitational mechanism, we might then expect that the ξ pdfs at the different radial locations would differ noticeably in the position of the mode, which is more reflective of the mean flow properties, rather than simply in the properties of the tails, which reflect the turbulent fluctuations. Velocity measurements in this flow would be necessary to address this issue conclusively.

C. Spectral analyses

Prior numerical studies of differential diffusion[12–15,17,18,20] have considered power spectra of ξ, or similar scalar difference variables, to gain insight into the structural characteristics of the differential diffusion fields, in particular the relative importance of different length scales. Kerstein *et al.*[12] developed a model for the ξ spectrum based on the well-known form of conventional scalar spectra at high Reynolds numbers (Fig. 11). Consider two scalars, where the scalar labeled with subscript "1" has the higher diffusivity. For sufficiently high Re, the spectrum for each scalar will show an extended inertial range where $E \propto k^{-5/3}$. For each scalar, there will then be a cutoff wavenumber k_i beyond which $E(k)$ quickly drops off due to diffusion; scalar 1 has a higher diffusivity, so $k_1 < k_2$, as shown in the figure. Kerstein *et al.* argued that fluctuations in scalar 1 become negligible (relative to fluctuations in scalar 2) for $k \gg k_1$, so the behavior of ξ is dominated by scalar 2, giving $E_\xi \approx E_2$, for large k. Those authors further contended that ξ fluctuations at the limit of small k are also small, because that wavenumber range is far from the molecular diffusive scales where the differential diffusion originates. The result is that E_ξ has a peak at a k value intermediate to the two cutoff wavenumbers. The position of the peak is presumed to scale with k_1, since k_1 can be viewed as establishing the disparity in spectral properties of the two scalars at high wavenumbers.

Figure 12 presents the spectra of our measured ξ, i.e., $E_d(k_d)$, determined from one-dimensional, radial ξ profiles through the jet. The quantities E_d and k_d are normalized by the jet exit diameter d. (No normalization is applied to the ξ values.) Shown are the power spectra at $x/d = 13$ for $\mathrm{Re}_0 = 1000$, 2500, and 3000, and at $x/d = 17$ for $\mathrm{Re}_0 = 2500$ and 3000. We applied a Hann window to the data profiles prior to computing the spectra. All of the measured ξ spectra in Fig. 12 resemble the spectra of conventional scalar variables more closely than they do the presumed E_ξ in Fig. 11. None of the measured E_d shows a peak at intermediate wavenumber values. At $x/d = 13$, a comparison of the spectra for the three Reynolds numbers (Fig. 12(a)) shows the continued

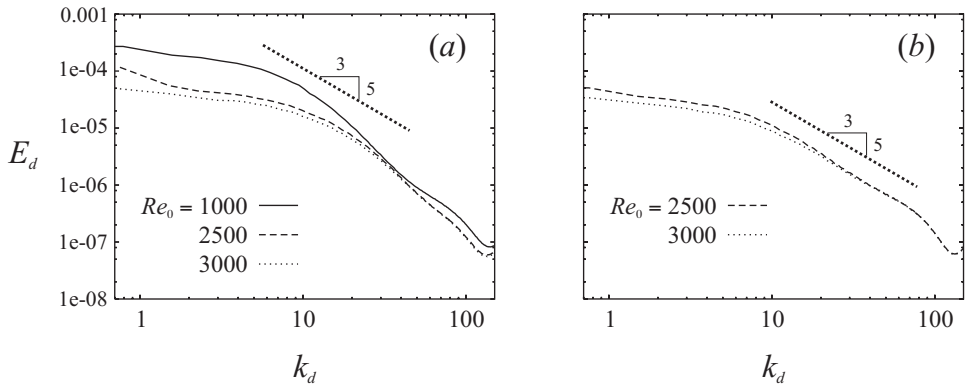

FIG. 12. The spectrum of ξ (E_d, normalized using the jet diameter), determined from one-dimensional radial profiles from the ξ fields, at (a) $x/d = 13$ for $\mathrm{Re}_0 = 1000$, 2500, and 3000, and (b) at $x/d = 17$ for $\mathrm{Re}_0 = 2500$ and 3000. The profiles at $x/d = 17$ show a distinct $k^{-5/3}$ inertial range.

TABLE III. Radial span of the one-dimensional samples used for determining the spectra shown in Fig. 12. The spectrum for $Re_0=1000$ at $x/d=13$ is symmetric about the jet centerline; all others span from the centerline outward. The quantity δ' is as defined in Sec. III A.

Re_0	$x/d=13$	$x/d=17$
1000	$(1.5\delta', 1.5\delta')$	—
2500	$(0, 2.1\delta')$	$(0, 1.8\delta')$
3000	$(0, 2.1\delta')$	$(0, 1.7\delta')$

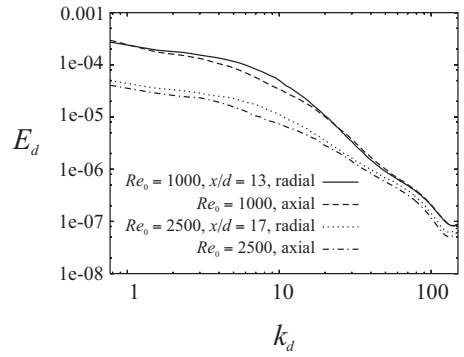

FIG. 13. Dependence of the ξ spectra on the sampling direction. Shown are the radial spectra for $Re_0=1000$ at $x/d=13$ and $Re_0=2500$ at $x/d=17$, as shown in Fig. 12, along with axial spectra along the jet centerline for $Re_0=1000$, computed from $x/d=12.2$ to 16.2, and for $Re_0=2500$, computed from $x/d=16.5$ to 20.6. There are effectively no differences between the radial and axial spectra.

effect of the relatively large ξ structures that characterize the laminar portion of the low Reynolds number jet, in that the $Re_0=1000$ spectrum has notably higher values in the low wavenumber range. Similarly, the $Re_0=2500$ spectrum has marginally higher values than the $Re_0=3000$ spectrum for small k, possibly reflecting a greater likelihood that laminar-like structures will be present at $Re_0=2500$, though the two spectra are in very good agreement beyond $k_d\approx 20$. At $x/d=17$, the spectra for $Re_0=2500$ and 3000 (Fig. 12(b)) both show a clear $k^{-5/3}$ inertial range that spans approximately one decade. This inertial range is not evident in the spectra at $x/d=13$, and suggests that the $x/d=17$ location is in an asymptotic range of the development of the ξ field.

Interpretation of spectra computed from spatial samples, such as those in Fig. 12, must recognize that the sampling region may span regions of the flow whose spectral properties may differ. Table III shows the radial span of the one-dimensional samples used to determine the spectra in Fig. 12. The samples all include the jet centerline, and extend to between $r/\delta'=1.5$ to 2.1 from the centerline, where δ' is as defined in Sec. III A. From Fig. 8, the maximum r/δ' values used for determining the spectra may be in regions where the ξ fluctuations are small. The spectral determination may therefore include, for example, large regions of ambient fluid where $\xi=0$, which could affect particularly the low-k parts of the spectra. To assess this possibility, Fig. 13 compares spectra computed along the jet centerline in the axial direction (for $Re_0=1000$ spanning from $x/d=12.2$ to 16.2, and for $Re_0=2500$ spanning from $x/d=16.5$ to 20.6) with radial spectra from similar axial locations. It is clear from the figure that there is no significant difference between the axial and radial spectra, so the results in Fig. 12 are not evidently affected by spatial inhomogeneity in the turbulence levels.

The results shown in Fig. 12 argue that the spectral properties of the jet ξ field are dominated by structures that arise in the near-nozzle portion of the flow, rather than by structures that form due to local molecular effects. The monotonic decay in the E_d spectra with increasing wavenumber is reminiscent of the cascade process describing conventional scalar mixing, where low wavenumbers describe energy input and high wavenumbers represent energy dissipation. In the context of the transport equation for ξ (Eq. (3)), the spectra of Fig. 12 indicate that the right side of the equation, which is a source term that introduces energy to the ξ field in the diffusive (high wavenumber) range, has a negligible effect on the spectral structure of the ξ field.

This view of the dominant role of near-field laminar ξ structures can also explain the observed differences in the spectra at $x/d=13$ and 17. At $x/d=13$, the spectra in the wavenumber range from $k_d\approx 10$ to 100 decays more rapidly than $k^{-5/3}$, with the steepest decay for $Re_0=1000$. This likely reflects that the large differential diffusion structures that form in the near-nozzle range have yet to be significantly broken up by the action of the turbulent cascade. Further downstream, in contrast, the presence of the inertial range implies that the turbulent cascade has attained a characteristic asymptotic state. This picture supposes that the spectral energy in the ξ field, characterized by ξ values that depart significantly from zero, is generated at relatively large scales, in the less turbulent parts of the flow, which is typically in the jet near field; subsequently, the ξ spectrum behaves similarly to that of conventional scalar fields. At no point in the measurement domain does the spectrum show signs of being significantly affected by energy input at high wavenumbers.

The form of the spectra in Fig. 12 stands in stark contrast to the results of certain prior computations and spectral analyses that considered isotropic turbulent mixing.[12,13,18,20] In those cases, large-scale spectral energy generation in the ξ field was effectively rendered negligible by assuming that the different scalars began with identical initial conditions in a fully developed turbulent field, so that no laminar regions were present where large ξ structures could form. It is important to note that in these simulations, the scalars were forced, either by introducing stochastic source terms to the scalar equations or by imposing mean scalar gradients. One simulation whose scalar difference spectrum resembles the present experimental result is the DNS of Yeung and Pope,[14] involving decaying isotropic turbulence. In that paper, the initial scalar difference spectra show an intermediate peak, as hypothesized by Kerstein *et al.*;[12] however, for later times, the spectra take on the monotonically decaying form seen in Fig. 12. The effect of forcing is apparently to generate, for the duration of the simulation, regions of high gradients in the individual scalars, which are regions in which differential diffusion can develop at the molecular scales. In a decaying simulation, the peak gradients will continually diminish, resulting in the gradual de-emphasis of the high-wavenumber production mechanism for ξ. (The Nilsen and Kosály[17] simu-

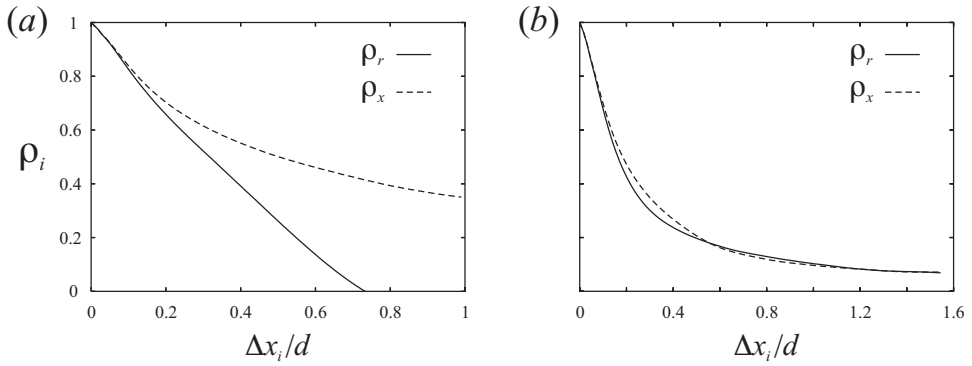

FIG. 14. Radial and axial ξ auto-correlations ρ_r and ρ_x, from the $\mathrm{Re}_0=1000$ jet, compiled in (a) the transitional region ($x/d=8$) and (b) the turbulent region ($x/d=13$). The auto-correlations at $x/d=8$ reflect the presence of the laminar ξ structures that are aligned with the axial direction. The downstream auto-correlations indicate that the ξ field rapidly approaches isotropy.

lation similarly addresses decaying turbulence, but does not show a monotonically decreasing ξ spectrum as in Fig. 12; Mydlarski (private communication) points out that the Nilsen and Kosály simulation spans an insufficient number of eddy-turnover times to manifest the spectral changes seen by Yeung and Pope.)

The agreement of the decaying turbulence simulation of Yeung and Pope with our observations can be explained by the present jet geometry and Reynolds number range. In particular, the jets studied here, with relatively modest Re_0, have a finite pretransition region in which molecular effects can play a dominant role, allowing significant differential diffusion to develop at relatively large scales. Post-transition, the small-scale scalar gradients generated by the turbulence are evidently insufficient to generate differential diffusion (at high wavenumbers) to a level comparable to that in the pretransition region. These results may have important implications for other flow systems where turbulence levels can vary significantly, for example, reacting flows that are subject to local laminarization in high-temperature regions. These regions of low turbulence intensity may allow significant local generation of low-wavenumber ξ structures even as the global flow Reynolds number is nominally high.

As mentioned earlier, there is no experimentally verified Reynolds number scaling for the magnitude of ξ fluctuations. The scaling derived by Kerstein *et al.*[12] was based on an assumed shape for the spectrum of ξ, and relied on the assumption that large-scale variance is negligible. The spectra shown in Fig. 12, which show significant large-scale energy in the ξ field, may make the expected scaling different from that predicted by Kerstein *et al.* The present measurements do not span a sufficient range of Reynolds numbers to allow direct determination of the proper scaling of the ξ fluctuations.

D. Structural properties of the ξ fields

Planar measurements such as these have the advantage of affording direct access to the spatial structure of the fields in question. This is important in the context of current simulation efforts for turbulent reacting flows, such as large-eddy simulation, which are rooted in the structural organization of the flows. In order to take proper account of differential diffusion in structure-based simulations, it will be necessary to develop an understanding of the structural properties, in addition to the statistical properties, of the differential diffusion.

Figure 14 shows the spatial auto-correlation function in both the radial and axial directions, ρ_r and ρ_x, respectively, computed on the centerline, at two different axial positions within the $\mathrm{Re}_0=1000$ jet. As mentioned previously, the flow does not have an asymptotically turbulent, self-similar form throughout the present measurement region, so these auto-correlations are useful for providing insight into the spatial organization of the differential diffusion fields in the developing region of the flow. At $x/d=8$ (Fig. 14(a)), which is in the transitional region, the auto-correlations show strong anisotropy, with $\rho_x \gg \rho_r$. This is consistent with the persistence of the characteristic laminar ξ structures, which are aligned in the axial direction. The auto-correlations at $x/d=13$ (Fig. 14(b)), in contrast, are very similar, indicating that the directional bias in the laminar portion of the ξ field is quickly removed by the turbulence. (Although the directional bias associated with the laminar structures is significantly reduced in moving from $x/d=8$ to $x/d=13$, recall from Fig. 12(a) that there remains significant spectral energy at low wavenumbers at $x/d=13$ for $\mathrm{Re}_0=1000$.) Further, the ρ_{x_i} for $x/d=13$ decay more rapidly with increasing separation Δx_i than for $x/d=8$, meaning that characteristic sizes of structures in the ξ field become smaller after the turbulent transition.

The auto-correlations in Fig. 15, for the $\mathrm{Re}_0=3000$ jet, indicate that the ξ field is nearly isotropic at both $x/d=13$ and 17. The ξ spectra in Fig. 12(b) show that an inertial range, possibly indicative of convergence to an asymptotic mixing state, develops between $x/d=13$ and 17. Isotropy in the ξ field thus appears to precede the convergence of its power spectrum. We hypothesized previously that the relatively large structures that are formed in the (pretransitional) near field of the jet provide the energy input to the scalar energy cascade. The auto-correlations for the low Re jet (Fig. 14) confirm the qualitative observation that these large structures tend to be aligned with the axial direction. The results for $\mathrm{Re}_0=3000$ (Fig. 15) then augment this observation by indicating that turbulent advection randomizes the orienta-

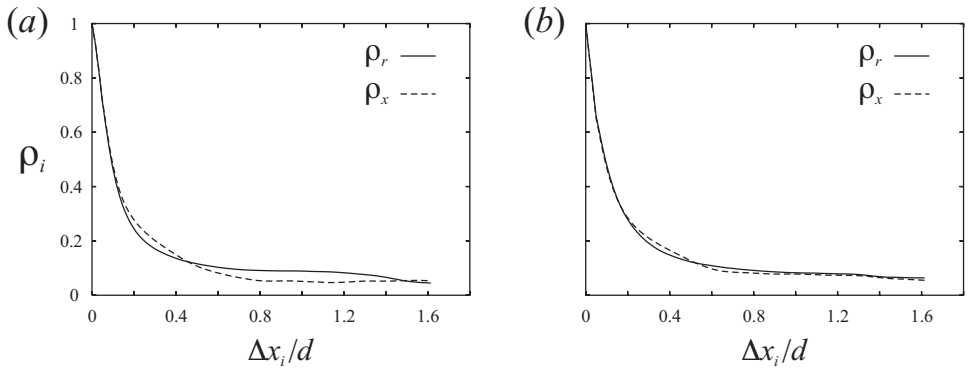

FIG. 15. Radial and axial ξ auto-correlations, from the $Re_0=3000$ jet, compiled at (a) $x/d=13$ and (b) $x/d=17$. The downstream ξ field is substantially isotropic.

tion of these structures before the turbulence breaks down the structures and initiates the asymptotic turbulent cascade.

We investigate further the structure of the differential diffusion by considering the spatial distribution of significant features in the ξ fields. In order to isolate these features we first compute the "scalar dissipation rate" of ξ; namely, $\chi \equiv \nabla\xi \cdot \nabla\xi$. In analogy with conventional scalar fields, structures with significant ξ values have a lamellar form. The method by which we isolate the individual dissipation layers in the χ field is adapted from Su and Clemens.[26] Figure 16 outlines the procedure. A sample ξ field from the $Re_0=1000$ jet is shown in Fig. 16(a), and its associated dissipation rate field is given in Fig. 16(b). (For these analyses of dissipation layers, we apply a 7×7 median filter to the original ξ fields.) We define dissipation layers as continuous surfaces of local maxima in the scalar dissipation field. The layer determination process begins by finding those points in the χ field that represent local maxima of the scalar dissipation in the direction of the scalar gradient vector. Any such points where χ is below the noise threshold are discarded. From the resulting field of local maxima, we identify layers as continuous structures spanning a minimum length of six pixels. This length criterion is applied as an additional noise-reduction measure. Figure 16(c) shows the field of dissipation layers corresponding to the given ξ field.

For each point on the identified dissipation layers (Fig.

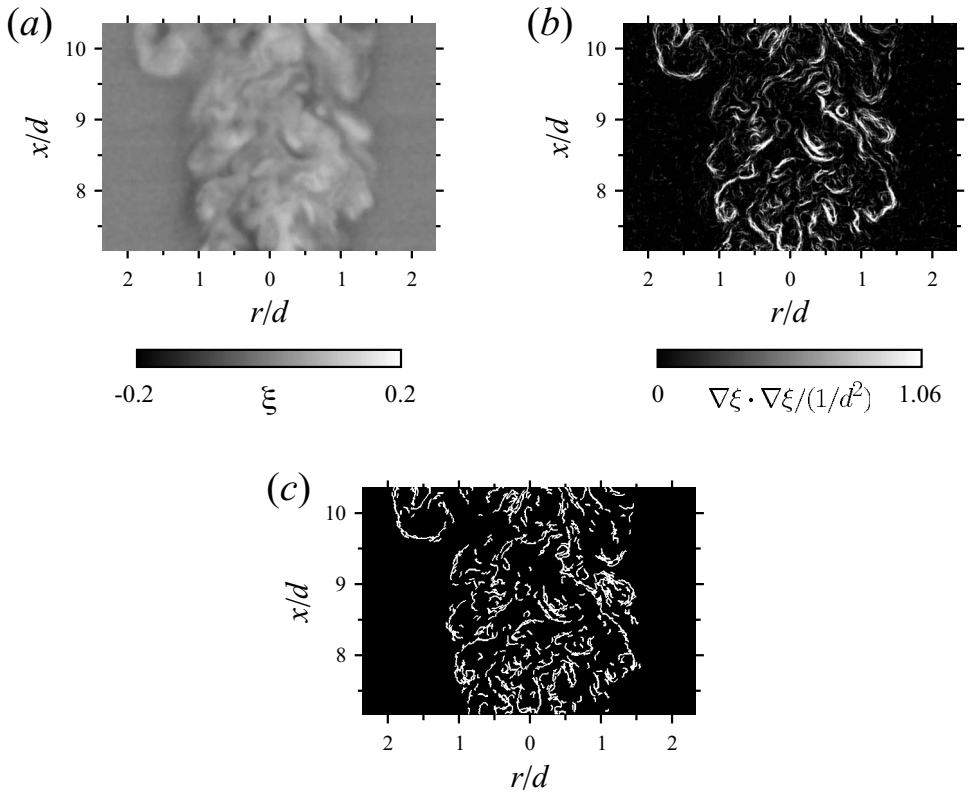

FIG. 16. (a) A sample ξ field from the $Re_0=1000$ jet, (b) the associated scalar dissipation rate field, i.e., $\chi \equiv \nabla\xi \cdot \nabla\xi$, and (c) distinct layers in the χ field. Identification of these layers provides a direct view of the spatial arrangement of significant structures in differential diffusion field.

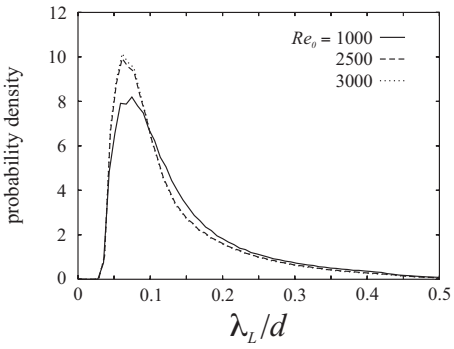

FIG. 17. Probability distributions of the thicknesses λ_L of the dissipation layers, identified as shown in Fig. 16. Distributions are shown for $Re_0=1000$, 2500, and 3000, and are compiled for the range of downstream positions $x/d=13\pm0.5$. Table IV presents the mean thicknesses computed from these distributions.

16(c)), we can determine the local thickness λ_L as the separation, in the direction normal to the layer, between points where the scalar dissipation rate drops to 20% of its peak value. Figure 17 shows probability distributions of λ_L (normalized by d) for $Re_0=1000$, 2500, and 3000, for the range of downstream positions spanning $x/d=12.5$ to 13.5. The distributions show a clear positive skewness, with a long tail representing the relatively infrequent occurrence of layers whose thickness is significantly larger than the most probable values. This is qualitatively similar to the layer thickness distributions measured for conventional scalar variables.[26] The mean λ_L values corresponding to the pdfs in Fig. 17, as well as for $Re_0=2500$ and 3000 in the downstream ranges $x/d=15\pm0.5$ and 19 ± 0.5, are compiled in Table IV. The mean λ_L values decrease with increasing Reynolds number, which is consistent with the Re dependence of the dissipation length scale λ_ν (Eq. (6)); however, λ_L also decreases with increasing x, which is at odds with the x dependence of λ_ν.

Equation (6) expresses that the relationship between the local flow outer scale δ and the dissipation scale λ_ν depends only on the local Reynolds number; equivalently, it can be viewed as a description of the turbulent cascade process whereby small-scale structures in the flow are generated through the breakdown of large structures. In the axisymmetric jet, the local Reynolds number is uniform throughout the flow, and the outer scale increases linearly with downstream distance, so the dissipation scale also goes as $\lambda_\nu \propto x$. If we view the differentially diffusing jet as consisting of two scalars whose distributions are identical upon encountering the turbulence, then the length scales that characterize the differential diffusion will relate directly to the turbulent diffusion scales themselves. This picture would require also that $\lambda_L \propto x$. The present observation that λ_L instead relates inversely to x can again be explained by the dominant role of the laminar regions in generating the differential diffusion structures. In particular, the significant ξ structures at any given downstream location should not be viewed as resulting from a cascade process originating at the local large scales, but rather as originating in the upstream laminar flow regions. The turbulent cascade thus operates in a Lagrangian sense on these ξ structures as the flow moves downstream, resulting in a gradual reduction in the characteristic differential diffusion length λ_L.

TABLE IV. Mean values of dissipation layer thicknesses λ_L computed for $Re_0=1000$, 2500, and 3000, in the downstream ranges $x/d=13\pm0.5$, 15 ± 0.5, and 19 ± 0.5. The values are expressed in terms of the jet diameter d and the local dissipation half-width δ'.

Re_0	$x/d=13\pm0.5$	$x/d=15\pm0.5$	$x/d=19\pm0.5$
1000	$0.140d$	—	—
	$0.0928\delta'$	—	—
2500	$0.131d$	$0.129d$	$0.124d$
	$0.0679\delta'$	$0.0548\delta'$	$0.0485\delta'$
3000	$0.129d$	$0.125d$	$0.120d$
	$0.0636\delta'$	$0.0509\delta'$	$0.0450\delta'$

The λ_L results from Table IV are resolution dependent, and therefore are also sensitive to the median filtering used here to suppress noise. Table V shows the effect of different median filter sizes on both the measured λ_L and the standard deviation of λ_L, for the $Re_0=3000$ jet at $x/d=13\pm0.5$ (of the results in Table IV, this is the furthest upstream location for the highest Re_0, and thus poses the most stringent resolution requirements). For the results in Table V, all cases use identical distributions of identified layers (such as those shown in Fig. 16(c)), determined using the 7×7 filter; the different filter sizes are applied in the direct computation of λ_L only. The noise in the raw measurements apparently leads to overestimation of λ_L, which is reduced with increasing effectiveness as the filter size increases from 3×3 to 5×5. For the larger filter sizes, the "blurring" effect of the filtering again causes the λ_L to be overestimated. The 7×7 median filter size (used for Table IV and in the remaining analysis) gives the smallest mean and standard deviation of λ_L, and is therefore optimal in the sense of reducing noise while minimizing the blurring of dissipation features.

Where the auto-correlation results from Figs. 14 and 15 provided information regarding the size and orientation of individual structures in the ξ field, we can investigate instead the spatial distribution of these structures by considering the probability of finding dissipation layers at different locations in the jet. Figure 18 shows radial profiles of the layer probability, for $Re_0=1000$, 2500, and 3000 at $x/d=13$, and for the higher two Reynolds numbers at $x/d=17$. (Specifically, the probability values shown represent the probability that one or more layers will intersect the square region, of side length $0.05d$, which is centered on the point in question in the imaging plane.) These profiles take on a clear bimodal form that is reminiscent of the ξ fluctuation profiles (Fig. 8). There are several other noteworthy aspects of these profiles. First, the peak values of the layer probabilities lie toward the centerline relative to the peak ξ fluctuations, which lie by definition at $r/\delta'=1$. Second, comparing the profiles for the different Reynolds numbers, the $Re_0=1000$ probability profile at $x/d=13$ shows much less distinct peaks than do the profiles at the higher Reynolds numbers, in that the centerline layer probability is nearly equal to the peak value; also, the layer probabilities are notably lower for $Re_0=3000$ than

TABLE V. Dependence of the layer thicknesses on the size of the median filter applied to the ξ fields, for the $Re_0=3000$ jet at $x/d=13\pm0.5$. Shown are the mean λ_L (and the standard deviation of λ_L) for median filter sizes from 3×3 up to 11×11. The 7×7 filter used to compile Table IV has the smallest mean and standard deviation of λ_L.

	3×3	5×5	7×7	9×9	11×11
λ_L	$0.147d$ $(0.122d)$	$0.136d$ $(0.104d)$	$0.129d$ $(0.089d)$	$0.169d$ $(0.115d)$	$0.204d$ $(0.130d)$

for $Re_0=2500$. It is somewhat surprising that the layer probabilities are relatively evenly distributed across the $Re_0=1000$ jet, given that the development of differential diffusion structures in the lower Reynolds number jet might be presumed to be more dominated by the large laminar structures in the near field, which reside on the edges of the jet (e.g., Fig. 3). A possible explanation is that, at this location in the $Re_0=1000$ jet, the layer probability profile reflects the local formation of differential diffusion structures (in less-turbulent regions) more than the turbulent advection of existing structures. At the higher Reynolds numbers (and further downstream), the bimodal probability profiles appear to correlate more distinctly with turbulent advection. The lower probability values for $Re_0=3000$ would then be the result of diminished generation of ξ structures, resulting from a lower likelihood of less-turbulent regions in the flow. The dominant role of turbulent advection, at higher Re and in the downstream regions, is again consistent with the inertial mechanism proposed in Sec. III A as being responsible for the characteristic mean ξ profiles in the turbulent flow regions.

IV. CONCLUSIONS

This paper describes quantitative, planar measurements of the differential diffusion variable ξ in a turbulent propane-helium jet issuing into air. The measurements employ planar laser Rayleigh scattering. Relatively few experimental measurements of differential diffusion have been reported in the literature. Prior quantitative analyses using experimental data have been confined to line or point measurements. There are a number of technical challenges in the present experimental method, arising both from the laser diagnostic technique and from the data reduction. Rayleigh scattering, particularly when measuring the subtle changes in gas concentrations resulting from differential diffusion, is characterized by relatively low signal levels and, therefore, suboptimal signal-to-noise ratio. This necessitates the careful implementation of data reduction procedures, which here includes an unusual background correction method. The data reduction process that determines ξ from the measured Rayleigh scattering signal also imposes strict requirements on the experimental conditions. Specifically, any departures of the initial composition of the jet from that where the scattering cross section of the jet is matched with that of air will result in significant errors in the calculation of ξ. Recognizing this sensitivity, we have implemented a calibration method that reduces the effective uncertainty of the mixture fraction by up to an order of magnitude.

The measurements reported here encompass jet exit Reynolds numbers between 1000 and 3000, corresponding to estimated outer-scale Reynolds numbers from 4300 to 13 000. In the near field, prior to the turbulent transition, the ξ field takes on a characteristic laminar form, in which a region of excess helium (relative to the initial helium-propane ratio) is present on the outer edge of the jet, with excess propane just to the inside of this region. This laminar structure is more pronounced at lower Reynolds number, though it is present to some degree in all cases. Further downstream, radial profiles of ξ take on a characteristic turbulent form that is a rough inverse of the laminar form; the jet outer edge is marked by a slight tendency to excess propane, with excess helium toward the center of the jet. This turbulent structure is observed for all of the Reynolds numbers considered, and its presence is, therefore, apparently

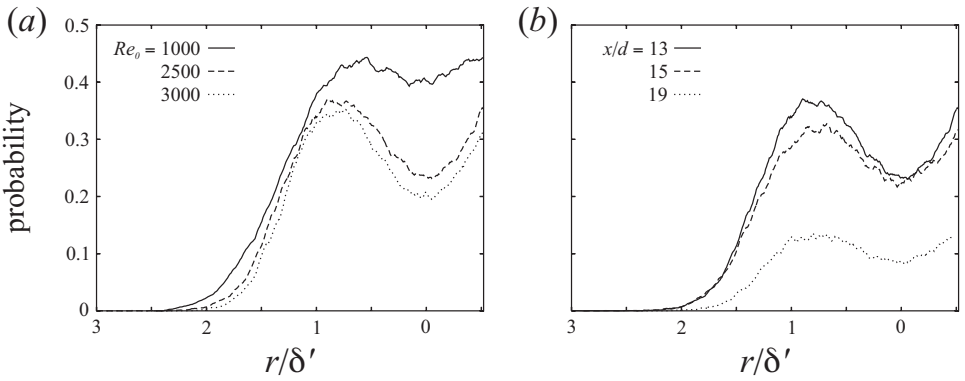

FIG. 18. Radial profiles of the probability of finding a dissipation layer at a given location in the flow, for (a) $Re_0=1000$, 2500, and 3000 at $x/d=13$ and (b) for $Re_0=2500$ $x/d=13$, 15, and 19. The radial coordinate is normalized by δ' (as defined in Sec. III A) for each Reynolds number individually. (Compare Fig. 9.)

independent of the degree to which the laminar structure of the ξ field pertains in the jet near field.

Other properties of the ξ field are consistent with the mixing of conventional scalar fields. Radial profiles of the ξ fluctuations show a bimodal form consistent with the profiles of conventional scalar fluctuations. For each Reynolds number, profiles from different downstream locations are self-similar, though the self-similar form is Re dependent (again, analogous to conventional scalars). The peak ξ'_{rms} values vary inversely with Re, though the properties of the present data do not allow a precise quantification of an inverse power-law dependence. Power spectra measured from the present ξ fields also provide an interesting comparison both with the spectra of conventional scalars, and with spectra determined from analyses and simulations of differential diffusion in isotropic turbulent flows. The form of the spectra found for differential diffusion in isotropic turbulence, in which there is a peak in a wavenumber range intermediate between the diffusive cutoffs of the individual scalars, is not reproduced in these measurements. Instead, our measured spectra are qualitatively consistent with conventional scalars, and display a $k^{-5/3}$ inertial range in the downstream portion of the measurement region.

Using these ξ measurements, we have also evaluated the structure of the ξ field by considering scalar "dissipation" fields, computed from ξ as $\chi \equiv \nabla\xi \cdot \nabla\xi$. Using these χ fields we measured the thicknesses λ_L of differential diffusion structures, and found that the λ_L values decrease with downstream distance, while the characteristic dissipation scales are well known to increase with downstream distance in the jet flow. Taken together, the ξ spectra, and the properties of the dissipation thickness λ_L, suggest a picture for differential diffusion in the jet in which relatively large structures where ξ departs significantly from zero are primarily generated in the laminar, near-field portion of the flow; these structures then are acted upon by the turbulent cascade in similar fashion to structures in conventional scalar fields as they advect downstream. The primary distinction between the evolution of the ξ field and conventional scalar fields is that large-scale energy generation is negligible in the ξ field in the downstream, turbulent part of the flow.

It is clear from these results for the axisymmetric jet, and from comparison with prior work that concerned isotropic turbulence, that the phenomenon of differential diffusion is fundamentally dependent on the nature of the underlying flow field. The jet flow considered here has a finite, nonturbulent pretransition region, so the turbulence intensity in the flow is not spatially uniform. This nonuniformity then has a defining effect on the resulting differential diffusion fields. The implications of this for realistic flows are significant. In practical combustion systems, for example, the ratio of extreme temperatures is over 7, and local Reynolds numbers can vary by a factor of 30, so the tendency of differential diffusion to develop in more laminar regions can be emphasized by local flow laminarization due to heat release. The observed properties of differential diffusion in such flow systems will likely differ noticeably from those in isotropic turbulent flows.

ACKNOWLEDGMENTS

This work is supported by the National Science Foundation through Grant No. CTS-0348208. The authors gratefully acknowledge the assistance provided by David Helmer in the experiments.

[1] M. C. Drake, M. Lapp, C. M. Penney, S. Warshaw, and B. W. Gerhold, "Measurements of temperature and concentration fluctuations in turbulent diffusion flames using pulsed Raman spectroscopy," Proc. Combust. Inst. **18**, 1521 (1981).
[2] R. W. Bilger, "Molecular transport effects in turbulent diffusion flames at moderate Reynolds number," AIAA J. **20**, 962 (1981).
[3] L. L. Smith, R. W. Dibble, L. Talbot, R. S. Barlow, and C. D. Carter, "Laser Raman scattering measurements of differential molecular diffusion in turbulent nonpremixed jet flames of H2/CO2 fuel," Combust. Flame **100**, 153 (1995).
[4] R. Hilbert and D. Thevenin, "Influence of differential diffusion on maximum flame temperature in turbulent nonpremixed hydrogen/air flames," Combust. Flame **138**, 175 (2004).
[5] R. W. Bilger and R. W. Dibble, "Differential diffusion effects in turbulent mixing," Combust. Sci. Technol. **28**, 161 (1982).
[6] A. R. Kerstein, R. W. Dibble, M. B. Long, B. Yip, and K. M. Lyons, "Measurement and computation of differential molecular diffusion in a turbulent jet," in Proc. Seventh Symp. on Turbulent Shear Flows, Stanford, CA, 21–23 August 1989, pp. 14.2.1–14.2.5.
[7] R. W. Dibble and M. B. Long, "Investigation of differential diffusion in turbulent jet flows using planar Rayleigh scattering," Combust. Flame **143**, 644 (2005).
[8] M. B. Long, S. H. Stårner, and R. W. Bilger, "Differential diffusion in jets using joint PLIF and Lorenz-Mie imaging," Combust. Sci. Technol. **92**, 209 (1993).
[9] J. R. Saylor and K. R. Sreenivasan, "Differential diffusion in low Reynolds number water jets," Phys. Fluids **10**, 1135 (1998).
[10] T. Lavertu, W. Pohl, S. Gaskin, and L. Mydlarski, "Punctual and planar measurements of differential diffusion in a turbulent jet," in Advances in Turbulence X: Proceedings of the 10th European Turbulence Conference, Trondheim, Norway, 2004, pp. 91–94.
[11] L. L. Smith, R. W. Dibble, L. Talbot, R. S. Barlow, and C. D. Carter, "Laser Raman scattering measurements of differential molecular diffusion in nonreacting turbulent jets of H2/CO2 mixing with air," Phys. Fluids **7**, 1455 (1995).
[12] A. R. Kerstein, M. A. Cremer, and P. A. McMurtry, "Scaling properties of differential molecular diffusion effects in turbulence," Phys. Fluids **7**, 1999 (1995).
[13] M. Ulitsky, T. Vaithianathan, and L. R. Collins,"A spectral study of differential diffusion of passive scalars in isotropic turbulence," J. Fluid Mech. **460**, 1 (2002).
[14] P. K. Yeung and S. B. Pope, "Differential diffusion of passive scalars in isotropic turbulence," Phys. Fluids A **5**, 2467 (1993).
[15] P. K. Yeung, "Multi-scalar triadic interactions in differential diffusion with and without mean scalar gradients," J. Fluid Mech. **321**, 235 (1996).
[16] A. Kronenburg and R. W. Bilger, "Modelling of differential diffusion effects in nonpremixed nonreacting turbulent flow," Phys. Fluids **9**, 1435 (1997).
[17] V. Nilsen and G. Kosály, "Differentially diffusing scalars in turbulence," Phys. Fluids **9**, 3386 (1997).
[18] P. K. Yeung, "Correlations and conditional statistics in differential diffusion: Scalars with uniform mean gradients," Phys. Fluids **10**, 2621 (1998).
[19] R. O. Fox, "The Lagrangian spectral relaxation model for differential diffusion in homogeneous turbulence," Phys. Fluids **11**, 1550 (1999).
[20] P. K. Yeung, M. C. Sykes, and P. Vedula, "Direct numerical simulation of differential diffusion with Schmidt numbers up to 4.0," Phys. Fluids **12**, 1601 (2000).
[21] J. C. Southerland, P. J. Smith, and J. H. Chen, "Quantification of differential diffusion in nonpremixed systems," Combust. Theory Modell. **9**, 365 (2005).
[22] A. Eckbreth, *Laser Diagnostics for Combustion Temperature and Species* (Abacus Press, Kent, UK, 1988).
[23] *Landolt-Börnstein Numerical Data and Functional Relationships in Science and Technology*, 6th ed., edited by J. Bartels, H. Borchers, H. Hausen, K.-H. Hellwege, Kl. Schäfer, and E. Schmidt (Springer, Berlin, 1962), Vol. 2.

[24]R. B. Bird, W. E. Stewart, and E. N. Lightfoot, *Transport Phenomena* (Wiley, New York, 1960).
[25]D. R. Dowling and P. E. Dimotakis, "Similarity of the concentration field of gas-phase turbulent jets," J. Fluid Mech. **218**, 109 (1990).
[26]L. K. Su and N. T. Clemens, "The structure of fine-scale scalar mixing in gas-phase planar turbulent jets," J. Fluid Mech. **488**, 1 (2003).
[27]C. J. Chen and W. Rodi, *Vertical Turbulent Buoyant Jets: A Review of Experimental Data* (Pergamon, Oxford, 1980).
[28]F. P. Ricou and D. B. Spalding, "Measurements of entrainment by axisymmetrical turbulent jets," J. Fluid Mech. **11**, 21 (1961).
[29]P. E. Dimotakis, "The mixing transition in turbulent flows," J. Fluid Mech. **409**, 69 (2000).
[30]D. B. Helmer and L. K. Su, "Experimental investigations of mixing in turbulent jets with buoyancy," AIAA Paper 2007–1314.